Measurements of Atmospheric Neutrinos and Antineutrinos in the MINOS Far Detector

Measurements of atmospheric neutrinos and antineutrinos in the MINOS far detector

P. Adamson,[7] C. Backhouse,[19] G. Barr,[19] M. Bishai,[3] A. S. T. Blake,[5] G. J. Bock,[7] D. J. Boehnlein,[7] D. Bogert,[7] S. V. Cao,[27] J. D. Chapman,[5] S. Childress,[7] J. A. B. Coelho,[6] L. Corwin,[13] D. Cronin-Hennessy,[16] I. Z. Danko,[20] J. K. de Jong,[19] N. E. Devenish,[25] M. V. Diwan,[3] C. O. Escobar,[6] J. J. Evans,[15] E. Falk,[25] G. J. Feldman,[9] M. V. Frohne,[10] H. R. Gallagher,[28] R. A. Gomes,[8] M. C. Goodman,[1] P. Gouffon,[22] N. Graf,[12] R. Gran,[17] K. Grzelak,[29] A. Habig,[17] J. Hartnell,[25] R. Hatcher,[7] A. Himmel,[4] A. Holin,[15] J. Hylen,[7] G. M. Irwin,[24] Z. Isvan,[20] D. E. Jaffe,[3] C. James,[7] D. Jensen,[7] T. Kafka,[28] S. M. S. Kasahara,[16] G. Koizumi,[7] S. Kopp,[27] M. Kordosky,[30] A. Kreymer,[7] K. Lang,[27] J. Ling,[3] P. J. Litchfield,[16,21] L. Loiacono,[27] P. Lucas,[7] W. A. Mann,[28] M. L. Marshak,[16] M. Mathis,[30] N. Mayer,[28,13] M. M. Medeiros,[8] R. Mehdiyev,[27] J. R. Meier,[16] M. D. Messier,[13] W. H. Miller,[16] S. R. Mishra,[23] J. Mitchell,[5] C. D. Moore,[7] L. Mualem,[4] S. Mufson,[13] J. Musser,[13] D. Naples,[20] J. K. Nelson,[30] H. B. Newman,[4] R. J. Nichol,[15] J. A. Nowak,[16] W. P. Oliver,[28] M. Orchanian,[4] R. B. Pahlka,[7] J. Paley,[1] R. B. Patterson,[4] G. Pawloski,[16,24] S. Phan-Budd,[1] R. K. Plunkett,[7] X. Qiu,[24] A. Radovic,[15] J. Ratchford,[27] B. Rebel,[7] C. Rosenfeld,[23] H. A. Rubin,[12] M. C. Sanchez,[14,1] J. Schneps,[28] A. Schreckenberger,[16] P. Schreiner,[1] R. Sharma,[7] A. Sousa,[9] B. Speakman,[16] M. Strait,[16] N. Tagg,[18] R. L. Talaga,[1] J. Thomas,[15] M. A. Thomson,[5] R. Toner,[9,5] D. Torretta,[7] G. Tzanakos,[2] J. Urheim,[13] P. Vahle,[30] B. Viren,[3] J. J. Walding,[30] A. Weber,[19,21] R. C. Webb,[26] C. White,[12] L. Whitehead,[11,3] S. G. Wojcicki,[24] K. Zhang,[3] and R. Zwaska[7]

(The MINOS Collaboration)

[1]*Argonne National Laboratory, Argonne, Illinois 60439, USA*
[2]*Department of Physics, University of Athens, GR-15771 Athens, Greece*
[3]*Brookhaven National Laboratory, Upton, New York 11973, USA*
[4]*Lauritsen Laboratory, California Institute of Technology, Pasadena, California 91125, USA*
[5]*Cavendish Laboratory, University of Cambridge, Madingley Road, Cambridge CB3 0HE, United Kingdom*
[6]*Universidade Estadual de Campinas, IFGW-UNICAMP, CP 6165, 13083-970, Campinas, SP, Brazil*
[7]*Fermi National Accelerator Laboratory, Batavia, Illinois 60510, USA*
[8]*Instituto de Física, Universidade Federal de Goiás, CP 131, 74001-970, Goiânia, GO, Brazil*
[9]*Department of Physics, Harvard University, Cambridge, Massachusetts 02138, USA*
[10]*Holy Cross College, Notre Dame, Indiana 46556, USA*
[11]*Department of Physics, University of Houston, Houston, Texas 77204, USA*
[12]*Department of Physics, Illinois Institute of Technology, Chicago, Illinois 60616, USA*
[13]*Indiana University, Bloomington, Indiana 47405, USA*
[14]*Department of Physics and Astronomy, Iowa State University, Ames, Iowa 50011, USA*
[15]*Department of Physics and Astronomy, University College London, Gower Street, London WC1E 6BT, United Kingdom*
[16]*University of Minnesota, Minneapolis, Minnesota 55455, USA*
[17]*Department of Physics, University of Minnesota-Duluth, Duluth, Minnesota 55812, USA*
[18]*Otterbein College, Westerville, Ohio 43081, USA*
[19]*Subdepartment of Particle Physics, University of Oxford, Oxford OX1 3RH, United Kingdom*
[20]*Department of Physics and Astronomy, University of Pittsburgh, Pittsburgh, Pennsylvania 15260, USA*
[21]*Rutherford Appleton Laboratory, Science and Technologies Facilities Council, OX11 0QX, United Kingdom*
[22]*Instituto de Física, Universidade de São Paulo, CP 66318, 05315-970, São Paulo, SP, Brazil*
[23]*Department of Physics and Astronomy, University of South Carolina, Columbia, South Carolina 29208, USA*
[24]*Department of Physics, Stanford University, Stanford, California 94305, USA*
[25]*Department of Physics and Astronomy, University of Sussex, Falmer, Brighton BN1 9QH, United Kingdom*
[26]*Physics Department, Texas A&M University, College Station, Texas 77843, USA*
[27]*Department of Physics, University of Texas at Austin, 1 University Station C1600, Austin, Texas 78712, USA*
[28]*Physics Department, Tufts University, Medford, Massachusetts 02155, USA*
[29]*Department of Physics, University of Warsaw, Hoża 69, PL-00-681 Warsaw, Poland*
[30]*Department of Physics, College of William & Mary, Williamsburg, Virginia 23187, USA*
(Received 17 August 2012; published 17 September 2012)

This paper reports measurements of atmospheric neutrino and antineutrino interactions in the MINOS Far Detector, based on 2553 live-days (37.9 kton-years) of data. A total of 2072 candidate events are observed. These are separated into 905 contained-vertex muons and 466 neutrino-induced rock-muons, both produced by charged-current ν_μ and $\bar{\nu}_\mu$ interactions, and 701 contained-vertex showers, composed mainly of charged-current ν_e and $\bar{\nu}_e$ interactions and neutral-current interactions. The curvature of muon tracks in the magnetic field of the MINOS Far Detector is used to select separate samples of ν_μ and $\bar{\nu}_\mu$

events. The observed ratio of $\bar{\nu}_\mu$ to ν_μ events is compared with the Monte Carlo (MC) simulation, giving a double ratio of $R^{\text{data}}_{\bar{\nu}/\nu}/R^{\text{MC}}_{\bar{\nu}/\nu} = 1.03 \pm 0.08(\text{stat}) \pm 0.08(\text{syst})$. The ν_μ and $\bar{\nu}_\mu$ data are separated into bins of L/E resolution, based on the reconstructed energy and direction of each event, and a maximum likelihood fit to the observed L/E distributions is used to determine the atmospheric neutrino oscillation parameters. This fit returns 90% confidence limits of $|\Delta m^2| = (1.9 \pm 0.4) \times 10^{-3}$ eV^2 and $\sin^2 2\theta > 0.86$. The fit is extended to incorporate separate ν_μ and $\bar{\nu}_\mu$ oscillation parameters, returning 90% confidence limits of $|\Delta m^2| - |\Delta \bar{m}^2| = 0.6^{+2.4}_{-0.8} \times 10^{-3}$ eV^2 on the difference between the squared-mass splittings for neutrinos and antineutrinos.

DOI: 10.1103/PhysRevD.86.052007 PACS numbers: 14.60.Pq

I. INTRODUCTION

It has now been firmly established by experiment that muon neutrinos produced by cosmic-ray showers in the atmosphere undergo oscillations. The data are well described by $\nu_\mu \rightarrow \nu_\tau$ neutrino oscillations, and measurements of the oscillation parameters have been made by Super-Kamiokande (SK) [1–3], MACRO [4], Soudan 2 [5], and MINOS [6,7]. The atmospheric neutrino results are strongly supported by long-baseline experiments, which observe corresponding oscillations in accelerator beams of muon neutrinos. Beam neutrino measurements have been made by K2K [8], T2K [9], and MINOS [10–12], The MINOS beam data analysis, which uses a two-flavor model of neutrino oscillations, returns best fit values of $|\Delta m^2| = (2.32^{+0.12}_{-0.08}) \times 10^{-3}$ eV^2 and $\sin^2 2\theta = 1.00_{-0.06}$ for the oscillation parameters [12].

The MINOS experiment has performed separate measurements of antineutrino oscillations [13–15] by identifying antineutrino interactions in the Fermilab NuMI accelerator beam [16]. A precision measurement of these oscillations has been made by operating the NuMI beam in a $\bar{\nu}_\mu$-enhanced configuration. Using the $\bar{\nu}_\mu$-enhanced data set, the $\bar{\nu}_\mu$ oscillation parameters are measured to be $|\Delta \bar{m}^2| = [2.62^{+0.31}_{-0.28}(\text{stat}) \pm 0.09(\text{syst})] \times 10^{-3}$ eV^2 and $\sin^2 2\bar{\theta} = 0.95^{+0.10}_{-0.11}(\text{stat}) \pm 0.01(\text{syst})$ [15]. Such studies are of interest, as an apparent difference between the ν_μ and $\bar{\nu}_\mu$ oscillation parameters could indicate new physics. In particular, separate ν_μ and $\bar{\nu}_\mu$ measurements can be used to study models of nonstandard neutrino interactions [17,18], and probe *CPT* symmetry in the neutrino sector [19,20].

The SK experiment has also studied oscillations in atmospheric neutrinos and antineutrinos. Although SK cannot distinguish ν_μ from $\bar{\nu}_\mu$ on an event-by-event basis, they have performed a statistical analysis of their data and the results are consistent with equal ν_μ and $\bar{\nu}_\mu$ oscillation parameters [21].

The MINOS experiment is able to study atmospheric neutrinos and antineutrinos separately using its 5.4 kton Far Detector, which is located 705 m underground (2070 m water equivalent) in the Soudan mine, Minnesota. At this depth, the incident flux of cosmic-ray muons is reduced by a factor of 10^6 relative to the surface. By applying a series of selection requirements, the cosmic-ray muon background can be reduced by a further factor of 10^6, yielding a clean sample of atmospheric neutrino signal events. The MINOS Far Detector is magnetized, which enables atmospheric $\nu_\mu + N \rightarrow \mu^- + X$ and $\bar{\nu}_\mu + N \rightarrow \mu^+ + X$ charged-current (CC) interactions to be separated based on the curvature of the muons.

MINOS has been collecting atmospheric neutrino data since 2003 and has previously published charge-separated analyses of contained-vertex muons [6] and neutrino-induced rock-muons [7,22], based on 418 and 854 live-days of data, respectively. Both samples are largely composed of atmospheric neutrino ν_μ and $\bar{\nu}_\mu$ CC interactions, which are identified by the presence of a primary muon track in the reconstructed event. For contained-vertex muons, the reconstructed interaction vertex is contained inside the fiducial volume of the detector. The sample includes both fully contained muons, which stop in the detector, and partially contained muons, which exit the detector. The muon track is typically accompanied by some vertex shower activity, generated by the hadronic system, which is used to fully reconstruct the neutrino energy. For neutrino-induced rock-muons, the reconstructed vertex is outside the fiducial volume. The selected muons enter the detector in an upward-going or horizontal direction and can be either stopping or through-going.

The atmospheric neutrino analysis presented here is based on an updated data set of 2553 live-days, collected between August 2003 and March 2011. The contained-vertex muon and neutrino-induced rock-muon samples have been combined into a single analysis, along with an additional sample of contained-vertex showering neutrinos, which are mainly composed of ν_e and $\bar{\nu}_e$ CC interactions and neutral-current (NC) interactions. The data are compared to the hypothesis of $\nu_\mu \rightarrow \nu_\tau$ and $\bar{\nu}_\mu \rightarrow \bar{\nu}_\tau$ two-flavor vacuum oscillations.

II. THE MINOS FAR DETECTOR

The MINOS Far Detector [23] is a steel-scintillator calorimeter, containing 486 octagonal planes of 2.54 cm thick steel, interleaved with planes of 1 cm thick extruded polystyrene scintillator and air gaps of 2.4 cm thickness. The planes are vertical, with a height of 8 m. Each scintillator plane is divided into 192 strips of width 4.1 cm,

aligned at ±45 degrees to vertical. The direction of the strips alternates from plane to plane. The scintillation light is collected using wavelength-shifting fibers, which are embedded in the strips. At the ends of each strip, the emitted light is transported by clear optical fibers to multi-anode photomultiplier tubes.

The detector comprises two supermodules, of length 14.8 m and 14.0 m, separated by a gap of 1.1 m. Each supermodule is magnetized toroidally to an average field of 1.3 T using a current loop that runs through a 25 cm diameter coil hole along the central axis of the supermodule and then returns below the supermodule. The MINOS coordinate system is right handed, with the y axis pointed vertically upwards and the z axis directed horizontally along the central axis of the detector, such that beam neutrinos have a forward-going z direction. The directions of the scintillator strips define a pair of diagonal axes $U = (x + y)/\sqrt{2}$ and $V = (-x + y)/\sqrt{2}$. Each strip provides a 2D spatial point in either the U-z or V-z coordinate systems, denoted the U and V views, respectively.

The vertical alignment of the planes presents a source of difficulty in separating contained-vertex atmospheric neutrinos from the cosmic-ray muon background. Steep cosmic-ray muons incident on the detector between two planes can travel a significant distance into the detector before entering the scintillator, and therefore appear as contained-vertex atmospheric neutrino events. To reduce the background, a scintillator veto shield has been constructed above the detector, and is used to tag cosmic-ray muons entering the detector. The veto scintillator modules are grouped into four sections, two per supermodule, with a double layer on the top surface of the detector, and single layers diagonally above and at each side of the detector. To prevent gaps, adjacent modules overlap each other. The majority of cosmic-ray muons pass through two layers of scintillator before entering the detector and can therefore be vetoed with high efficiency.

The veto shield is used to reject cosmic-ray muon background in the selection of contained-vertex tracks and showers. An event is rejected if any activity is observed in the section of shield above the event vertex within a time window of ±50 ns. The shield efficiency is determined using samples of cosmic-ray muons from across the entire data set. The fraction of cosmic-ray muons vetoed by the shield is measured to be 96.6% ± 0.3%(syst). The systematic uncertainty is obtained by modifying the criteria used to select the cosmic-ray muon samples and calculating the resulting variation in shield efficiency.

At each stage of the contained-vertex event selection, the cosmic-ray muon background predictions are derived directly from the data by scaling down the observed distributions of vetoed events according to the measured shield efficiency. A small fraction of the atmospheric neutrino signal is also vetoed as a result of accidental coincidence with noise in the shield. The loss of signal is determined to be 1.0% ± 0.2%(syst), found by overlaying samples of veto shield data on simulated atmospheric neutrino events. The systematic uncertainty reflects the time-dependent variations in the veto shield data rates.

Since March 2005, the MINOS Far Detector has been used to study neutrino interactions from the Fermilab NuMI accelerator beam. The beam neutrinos are identified in the data by searching in 100 μs time windows, extrapolated from the beam spill times. These windows, which correspond to approximately 0.01% of the Far Detector live time, are removed from the atmospheric neutrino analysis. For the majority of running, the detector has been magnetized to focus forward-going negatively charged muons from beam neutrino interactions. However, the magnetic field was reversed during the $\bar{\nu}_\mu$-enhanced beam running, and also for a period of several months prior to beam start-up, for the purpose of studying the cosmic-ray muon charge ratio [24].

Only data collected with both the main detector and veto shield fully operational are used in the analysis. The final data set corresponds to 2553 live-days, an exposure of 37.9 kton-years.

III. ATMOSPHERIC NEUTRINO MONTE CARLO SIMULATION

The MINOS Monte Carlo (MC) simulation uses separate programs to generate contained-vertex atmospheric neutrino interactions inside the Far Detector and neutrino-induced muons from interactions in the surrounding rock. For contained-vertex atmospheric neutrino interactions, the NEUGEN3 simulation [25] is used to generate the interactions and hadronic final states. The transport of hadronic particles is then modeled using the GCALOR simulation [26]. For neutrino-induced rock-muons, the NUANCE generator [27] is used, with the GRV94 parton distribution functions [28]. The NUANCE simulation then propagates the muons from the rock to the edges of the detector. For both Monte Carlo samples, a GEANT3 [29] simulation of the Far Detector is used to model particle transport and detector response.

For contained-vertex atmospheric neutrino events, the simulation uses the flux calculation of Barr *et al.* [30] (Bartol 3D). For neutrino energies below 10 GeV, this calculation is based on a 3D simulation, with separate flux tables provided for the cases of solar minimum and solar maximum. Above 10 GeV, a 1D simulation has been used and a single set of flux tables is provided. For neutrino-induced rock-muons, where the majority of parent neutrinos have energies greater than 10 GeV, the simulation uses the earlier 1D calculation by the Bartol group [31] (Bartol 1D). The rock-muons are then reweighted as a function of their parent neutrino energy and zenith angle using the ratio of the Bartol 3D and Bartol 1D fluxes. Both the contained-vertex and rock-muon samples use distributions of neutrino production height obtained from

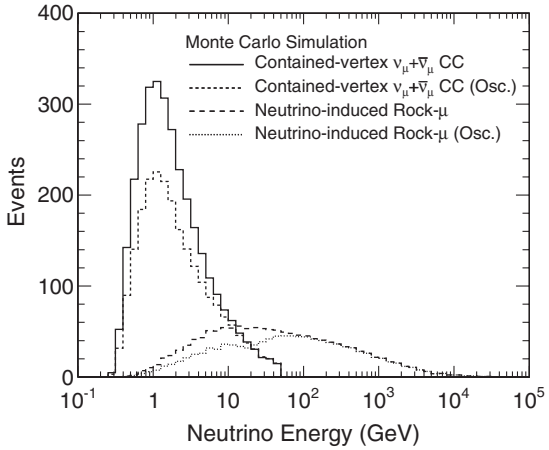

FIG. 1. The simulated atmospheric neutrino energy spectrum in the MINOS Far Detector for 2553 live-days of data. Separate distributions are plotted for contained-vertex neutrino interactions and neutrino-induced rock-muons showing the predictions for the case of no oscillations, and for oscillations with $\Delta m^2 = 2.32 \times 10^{-3}$ eV^2 and $\sin^2 2\theta = 1.0$. The contained-vertex neutrino interactions are generated in the range 0.2–50 GeV, with a median value of 2 GeV; the neutrino-induced rock-muons range up to neutrino energies of 10 TeV, with a median value of 50 GeV. The effect of $\nu_\mu \rightarrow \nu_\tau$ oscillations is visible for neutrino energies below 100 GeV.

a separate simulation of cosmic-ray interactions in the atmosphere and parametrized in terms of neutrino energy and zenith angle [5].

The Far Detector data set spans a significant fraction of the full solar cycle. For atmospheric neutrinos above 500 MeV (the MINOS energy threshold), the predicted neutrino interaction rate is 7% higher at solar minimum than solar maximum. These solar cycle effects are accounted for by taking a weighted average of the Bartol 3D fluxes calculated at solar minimum and solar maximum. The variation of solar activity over time is determined by parametrizing available atmospheric neutron data from the CLIMAX experiment [32]. Combining these data with the Far Detector running periods, the fluxes at solar minimum and solar maximum are combined in proportions 70% and 30%, respectively.

Figure 1 shows the simulated atmospheric neutrino energy spectrum for contained-vertex neutrino interactions and neutrino-induced rock-muons, plotted for the case of no oscillations, and for oscillation parameters of $\Delta m^2 = 2.32 \times 10^{-3}$ eV^2 and $\sin^2 2\theta = 1.0$ [12]. These oscillation parameters are also used to calculate predicted atmospheric neutrino event rates in Secs. V and VI of this paper.

A. Systematic uncertainties in atmospheric neutrino simulation

The predicted atmospheric neutrino event rates have large uncertainties arising from the atmospheric neutrino flux and interaction models. The Bartol group has carried out a detailed study of the systematic uncertainties in their 3D flux model [33]. These flux uncertainties have also been studied by comparing the Bartol model with the alternative 3D calculations of Battistoni *et al.* [34] and Honda *et al.* [35]. The systematic uncertainties used in this analysis are based on the results of the Bartol study but are also found to cover the differences between the different flux models.

The dominant source of uncertainty in the overall rate of contained-vertex neutrinos and neutrino-induced rock-muons is the systematic uncertainty in the normalization of the atmospheric neutrino flux simulation. This overall uncertainty increases with neutrino energy due to rising uncertainties in the primary cosmic-ray flux and hadroproduction models. For contained-vertex neutrinos, which have a median energy of 2 GeV and lie primarily below 10 GeV, an overall uncertainty of 15% is applied in this analysis. For neutrino-induced rock-muons, where the parent neutrino has a median energy of 50 GeV, with an energy spectrum that ranges up to 10 TeV, a larger uncertainty of 25% is applied.

At low neutrino energies, many of the systematic uncertainties in the flux model cancel in the ratios of different flux components. In the 1–5 GeV region, the uncertainties in the $(\nu_\mu + \bar{\nu}_\mu)/(\nu_e + \bar{\nu}_e)$ and $\nu_\mu/\bar{\nu}_\mu$ flux ratios, and in the up-down ratio of upward-going neutrinos to downward-going neutrinos, are calculated to be smaller than 5% [33]. For the analysis presented here, the uncertainty in the $\nu_\mu/\bar{\nu}_\mu$ ratio is of greatest importance. At energies below 10 GeV, cosmic-ray hadroproduction predominantly yields pions, with each charged pion producing a single pair of ν_μ and $\bar{\nu}_\mu$ in its decay chain. Therefore, the $\nu_\mu/\bar{\nu}_\mu$ ratio approaches unity, with a high degree of cancellation in its systematic uncertainty. For the contained-vertex atmospheric neutrino sample, a conservative uncertainty of 4% is placed on this ratio. At energies above 10 GeV, the cancellations in the ratio quickly diminish, as the large uncertainty in the kaon component of hadroproduction becomes a significant factor, and an increasing fraction of atmospheric muons strike the ground before decaying. Therefore, for the neutrino-induced rock-muon sample, a larger uncertainty of 10% is placed on the $\nu_\mu/\bar{\nu}_\mu$ ratio.

Additional systematic uncertainties in the predicted atmospheric neutrino event rate arise from the neutrino interaction model. The uncertainty in the total ν_μ CC cross-section peaks at 8% in the 1–5 GeV region [36], corresponding to the transition region between the models of quasielastic and resonance neutrino interactions. At higher energies, where deep inelastic interactions are dominant, the total interaction cross section is well constrained by experiment, and the uncertainty falls to 2%. For antineutrinos, where there is limited experimental data below 5 GeV, the predicted $\bar{\nu}_\mu$ CC cross section has a larger uncertainty. For the analysis presented here, an

energy-dependent systematic uncertainty band on the $\nu_\mu/\bar{\nu}_\mu$ cross-section ratio has been calculated by varying the input parameters to the NEUGEN3 interaction model according to their given uncertainties [37]. The average uncertainty in the $\nu_\mu/\bar{\nu}_\mu$ cross-section ratio is then calculated by integrating across this uncertainty band, weighting each bin of neutrino energy by the predicted rate of atmospheric neutrino ν_μ and $\bar{\nu}_\mu$ CC interactions. For the contained-vertex neutrino sample, this procedure yields an overall uncertainty of 8.5%. For the neutrino-induced rock-muon sample, where the majority of events are produced by deep inelastic neutrino interactions, the calculation returns a smaller uncertainty of 4%.

The atmospheric neutrino event rate at the Soudan mine has been previously measured by the Soudan 2 experiment. The Soudan 2 analysis of atmospheric electron neutrinos indicates that the predicted interaction rates obtained by combining the Bartol 3D flux model and NEUGEN cross-section model should be scaled by 0.91 ± 0.07 [5]. However, although the Soudan 2 and MINOS detectors are located at the same site, Soudan 2 has a lower neutrino energy threshold of 300 MeV, compared with 500 MeV for MINOS. An analysis of contained-vertex showers from atmospheric neutrinos by MINOS, based on 418 live-days of data, yields a scale factor of $1.08 \pm 0.12(\text{stat}) \pm 0.08(\text{syst})$ [38]. The systematic uncertainties applied in this analysis cover both these measurements.

IV. EVENT RECONSTRUCTION

The data are reconstructed using an algorithm which identifies the track and shower topologies in each event [39]. Reconstructed tracks typically contain hits in one strip per plane and are principally produced by muons; reconstructed showers contain hits in multiple strips per plane and are produced by hadronic and electromagnetic particles.

Initially, the particle tracks and showers are reconstructed independently in each of the U and V views; these 2D views are then matched to generate a 3D event. A Kalman filter algorithm is used to determine the trajectory of each muon track, accounting for energy loss in the detector and curvature in the magnetic field [40]. This algorithm also reconstructs the start and end points of each track, which are distinguished using timing information. For tracks where the end point lies inside the fiducial volume, the muon momentum is reconstructed from the measured track length; for exiting tracks, the momentum is obtained from the fitted track curvature. In both cases, the fitted curvature is used to determine the muon charge sign. For atmospheric neutrino events containing a reconstructed track, the interaction vertex is given by the start point of the track; if there is only a reconstructed shower, the vertex is given by the centroid of the shower.

The propagation direction of each muon along its reconstructed track is determined using timing information. The MINOS Far Detector has a single-hit timing resolution of approximately 2.5 ns, which enables the muon direction to be reconstructed with high purity for tracks spanning ten or more scintillator planes. The Far Detector timing system is calibrated using cosmic-ray muons, which are used to determine the time offsets in each readout channel and to correct for shifts in these offsets resulting from swapped readout components [39].

The detector is calibrated using a combination of LED light injection and the average pulse height response of each strip using cosmic-ray muons [23]. A minimum-ionizing muon passing through a scintillator strip at normal incidence generates a combined signal of approximately 10 photoelectrons (PEs). The selection of contained-vertex tracks and showers makes use of the energy profile of events.

For contained-vertex atmospheric ν_μ and $\bar{\nu}_\mu$ events, the emitted muon is typically accompanied by some reconstructed shower activity at the interaction vertex, produced by the hadronic system. The total hadronic energy is determined by summing the calibrated pulse heights in the reconstructed shower. For low energy showers, large fluctuations can occur, degrading the hadronic energy resolution. To reduce the size of these fluctuations, the pulse heights are first raised to a power before being summed together. The exponent used in this procedure is increased as a function of shower energy from a minimum of 0.25 at the lowest shower energies to a maximum of 1.0 for shower energies above 18 GeV [41]. Studies of simulated atmospheric neutrinos show that, relative to a linear summation of pulse heights, the hadronic energy resolution improves from 55% to 45% for reconstructed showers in the 1 GeV region.

V. EVENT SELECTION

An initial selection is applied to all events, ensuring a good reconstruction quality. The selected events are then separated into a tracklike sample containing reconstructed tracks that span 8 or more planes, and a showerlike sample containing reconstructed showers that span 4 or more planes. The tracklike sample is used for the selection of contained-vertex muons and neutrino-induced rock-muons; the showerlike sample is used for the selection of contained-vertex showers. Initially, 2% of events are placed in both the tracklike and showerlike samples. Any duplicate events are removed from the showerlike sample after the full selection has been applied. After the initial selection, the observed event rate is 55 000 events/day, dominated by cosmic-ray muons. The corresponding predicted atmospheric neutrino rates are 0.8 events/day from contained-vertex interactions, and 0.3 events/day from neutrino-induced rock-muons, after accounting for oscillations.

The atmospheric neutrino signal is separated from the cosmic-ray background using two characteristic signatures

of atmospheric neutrino interactions: either a reconstructed vertex inside the fiducial volume or a reconstructed upward-going or horizontal muon trajectory. A set of requirements on event containment and topology is first applied to select contained-vertex tracks and showers, using the veto shield to reduce the cosmic-ray muon background. A set of requirements on event timing information and length is then applied to select upward-going and horizontal muons produced by neutrino interactions in the detector or surrounding rock. The full selection is described in the following sections.

A. Selection of contained-vertex tracks

The contained-vertex track selection criteria identify ν_μ and $\bar{\nu}_\mu$ CC atmospheric neutrinos. For this sample, the veto shield selection is first used to reduce the level of cosmic-ray muon background. A set of containment and topology selection criteria are then applied to the remaining tracks. For each track, the reconstructed trajectory has two ends, corresponding to the first and last scintillator hits on the track. Since cosmic-ray muons are incident from above, the majority of these selection criteria are applied at the upper end of the track. The following selection criteria are applied [39,42,43]:

(1) *Fiducial cuts.*—The reconstructed track vertex is required to lie within a fiducial volume starting 0.2 m inside any edge of the detector, 5 planes from the ends of each supermodule, and 0.4 m from the center of the coil hole. To reject cosmic-ray muons that enter the detector through the coil hole, the coil cut is increased to 1 m in the first and last 20 planes of the detector. In addition, if the vertex is reconstructed at the lower end of the track from timing information, these selection criteria are also applied at the upper end of the track.

(2) *Trace cut.*—The cosmic-ray muons that pass the fiducial requirements typically enter the detector at a small angle to the planes, and can travel a significant distance through the detector before entering the scintillator. However, the distance traveled along the z axis is typically small, and so the background can be reduced by placing a minimum requirement on this distance. For each event, a detector entry point is estimated by extending the reconstructed trajectory at the upper end of the track upwards to the edge of the detector. The displacement along the z axis, Δ_Z, between the entry point and upper end of the track is then calculated (this quantity is referred to as the ''trace''). Figure 2 shows the predicted and observed distributions of the trace variable. The cosmic-ray muon background is peaked towards low values, whereas the atmospheric neutrino signal distribution has a flatter distribution. To reduce the background, events are required to satisfy $\Delta_Z > 0.5$ m.

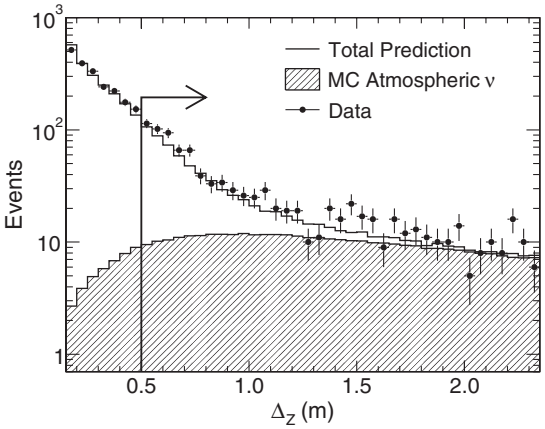

FIG. 2. Distributions of the trace variable, Δ_Z, for contained-vertex tracks. This estimates the distance in z traveled by a cosmic-ray muon inside the detector before first entering the scintillator. The hatched histogram shows the simulated prediction for the atmospheric neutrino signal; the solid line shows the predicted total rate, given by the sum of the signal and the cosmic-ray muon background; the points show the observed data. The background distribution is peaked towards low values of Δ_Z, and the arrow indicates the selection applied to reduce the background.

(3) *Topology cuts.*—The cosmic-ray muon background events that pass the trace cut typically travel a significant distance in a single steel plane and its associated air gap before entering the scintillator. A number of these cosmic-ray muons undergo significant bending in the magnetic field, and some muons reverse the horizontal component of their direction. As a result, the reconstruction may miss the first hit on the track or underestimate the steepness of the track. These events are characterized by clusters of hits above the upper end of the reconstructed track. To reduce this background, the charge-weighted mean and rms displacements of strips, denoted $\langle \Delta_{UV} \rangle$ and $\langle \Delta_{UV}^2 \rangle^{\frac{1}{2}}$, are calculated separately in the U and V views for a ± 4 plane window around the upper end of the track. Events are rejected if $\langle \Delta_{UV} \rangle > 0.25$ m, indicating that significant energy has been deposited above the track, or if $\langle \Delta_{UV}^2 \rangle^{\frac{1}{2}} > 0.5$ m, indicating that there was significant scatter at the upper end of the track. A set of 3D displacements is also calculated using the same ± 4 plane window, by combining all possible pairs of U and V strips in adjacent scintillator planes. The maximum 3D displacement from the upper end of the track, $\Delta_R^{\max}$, is then calculated, and events are rejected if $\Delta_R^{\max} > 1.25$ m.

(4) *Pulse height and direction cuts.*—The cosmic-ray muon background is also characterized by large deposits of energy at the upper end of the track, due to the long distance traveled in the first plane. This background is reduced by finding the maximum pulse

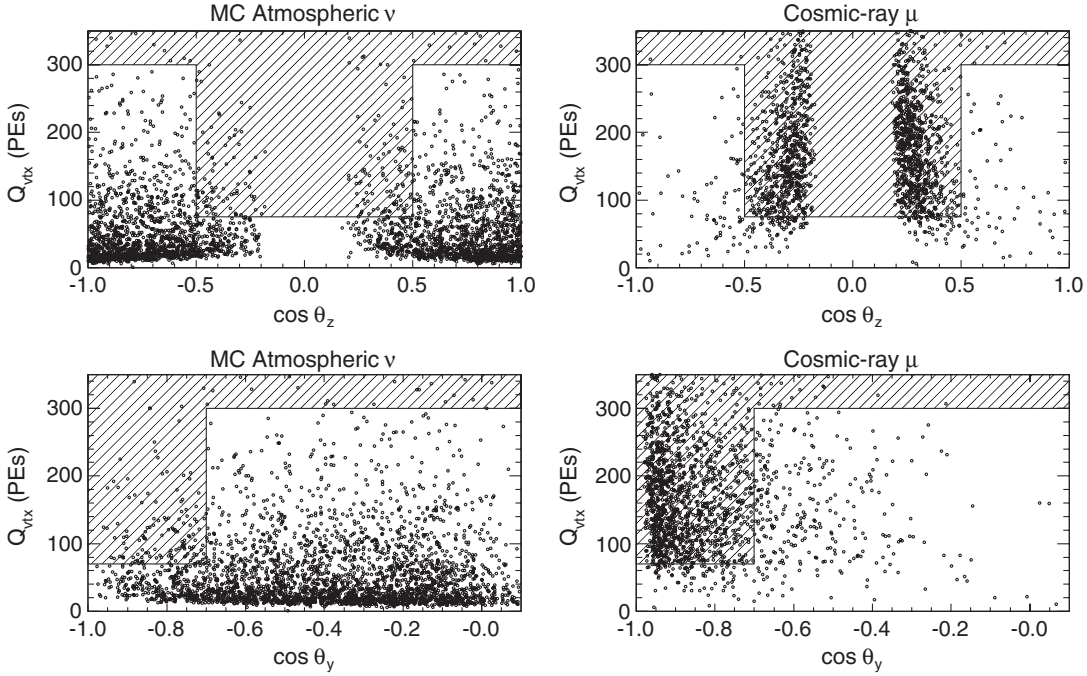

FIG. 3. Distributions of the pulse height at the upper end of the track ($Q_{\rm vtx}$), plotted against the z component ($\cos\theta_z$) and y component ($\cos\theta_y$) of the downward track direction. The distributions are plotted for contained-vertex muons that pass the trace and topology requirements and span fewer than 25 planes. The plots on the left show simulated atmospheric neutrinos; those on the right show the cosmic-ray muon background. The background events are associated with large pulse heights and directions parallel to the vertically aligned scintillator planes. The hatched area is the region rejected by the pulse height and direction selection criteria as part of the topology requirements. Note that the requirement of a track spanning ≥ 8 planes causes the acceptance to drop to zero as $|\cos\theta_z|$ approaches 0, and as $\cos\theta_y$ approaches -1.

height, $Q_{\rm vtx}$, in a ± 4 plane window around the upper end of the track. Events are rejected if $Q_{\rm vtx} > 300$ PEs. The $Q_{\rm vtx}$ requirement is tightened to 75 PEs if the track is both short, spanning fewer than 25 planes, and steep, satisfying $\cos\theta_y > 0.7$ or $|\cos\theta_z| < 0.5$. Here, θ_y and θ_z are taken as the angles between the reconstructed trajectory at the upper end of the track, and the y and z axes, respectively. Figure 3 shows the predicted signal and background distributions of $Q_{\rm vtx}$ as a function of θ_y and θ_z for the short tracks, indicating the selection requirements applied to separate the atmospheric neutrino signal from the cosmic-ray muon background.

The track containment requirements yield 801 events from the data. This compares with total predictions of 934 ± 134 events for no oscillations, and 698 ± 99 events for oscillations with $\Delta m^2 = 2.32 \times 10^{-3}$ eV^2 and $\sin^2 2\theta = 1.0$. The uncertainties in these predictions are dominated by the 15% uncertainty in the overall normalization of the contained-vertex Monte Carlo simulation. The combined ν_μ and $\bar{\nu}_\mu$ CC components form 92% of the total predicted event rate before oscillations. This component oscillates in the two-flavor model and therefore represents the signal in the oscillation analysis. The combined $\nu_e + \bar{\nu}_e$ CC and NC components, which do not oscillate in the two-flavor model, form a 5% background. The cosmic-ray muon prediction of 34 ± 3 events corresponds to a 3% background level.

B. Selection of upward-going and horizontal tracks

For upward and horizontal angles, where the rock overburden exceeds 14 000 m water-equivalent, the absorption of cosmic-ray muons by the earth is sufficiently high that the observed flux of muons is dominated by atmospheric muon neutrino interactions [44]. At the Soudan mine, this corresponds to zenith angles in the range $\cos\theta_z \leq 0.14$ [45]. Therefore, upward-going and horizontal muons in the MINOS Far Detector provide a signature for atmospheric neutrinos.

Upward-going and horizontal muons are selected based on the reconstructed zenith angle at the track vertex. The direction of muon propagation along the track is reconstructed using timing information. This is then used to distinguish between the track vertex and end points. The reconstructed track vertex can either be inside or outside the fiducial volume. Hence, this sample of events provides a source of both contained-vertex muons and neutrino-induced rock-muons.

To determine the track direction from timing information, two linear fits are applied to the measured times of the track hits, as a function of their distance along the track. The gradients are constrained to be $\pm 1/c$, corresponding

to forward and backward propagation along the track at the speed of light, c. The hits are weighted as a function of pulse height to account for the variation in the single-hit timing resolution, which is better for larger pulse heights due to increased photon statistics. For each propagation direction, the goodness of the timing fit is given by its rms timing residual. The smaller of the two rms values is labeled r_L, and the larger is labeled r_H. The propagation direction is determined by the timing fit with the smaller rms residual.

The neutrino-induced muons must be separated from a high background of cosmic-ray muons whose direction is misreconstructed. To ensure that the track direction is reconstructed unambiguously, the following selection criteria are applied:

(1) *Topology cuts.*—To ensure that there are sufficient hits on the track for the zenith angle to be reconstructed accurately, and the propagation direction determined unambiguously, reconstructed tracks are required to span more than 15 planes and to travel more than 1.5 m. For upward-going tracks, the track vertex point is required to lie below the track end point, or, to account for possible track curvature, no more than 0.5 m above it. For downward-going tracks, the track vertex requirement is reversed.

(2) *Timing cuts.*—To ensure that the muon propagation direction is identified unambiguously from timing information, a set of selection requirements are placed on the quality of the linear timing fits. The difference between the two rms residuals is required to satisfy $r_L - r_H < -1.66$ ns, a significant fraction of the detector timing resolution. In addition, an upper requirement of $r_L < 4.66$ ns is placed on the smaller residual and a lower requirement of $r_H > 3.66$ ns is placed on the larger residual. The ratio between the best fit rms residual, r_L, and the track length, l, also provides a means of selecting events with well-measured timing information. Events are required to satisfy $r_L/(l/c) < 0.577$.

These selection criteria identify clean samples of both upward-going and downward-going muons from the data. As a check on the quality of separation between these two samples, an additional unconstrained linear timing fit is applied to the selected events. The measured times along the track are fitted as a function of their upward distance along the track. The fits return a gradient, $1/v$, where v is the reconstructed velocity. Figure 4 shows the distribution of the normalized gradient, $1/\beta \equiv 1/(v/c)$. A good separation is achieved between the upward-going events, dominated by neutrino-induced muons, and the downward-going events, dominated by the cosmic-ray muon background.

Figure 5 shows the distribution of reconstructed zenith angle for the selected events. In the region $\cos\theta_z > 0.10$, the event rate falls steeply with zenith angle, as the rapidly increasing rock overburden reduces the incident flux of cosmic-ray muons. In the region $\cos\theta_z < 0.10$, the event rate flattens and becomes approximately constant, as neutrino-induced muons become the dominant flux component. A residual background arises from low momentum cosmic-ray muons that deflect significantly due to multiple Coulomb scattering in the rock and enter the detector in a horizontal direction. To minimize the cosmic-ray muon background, the selected sample of upward-going and horizontal muons is required to satisfy: $\cos\theta_z < 0.05$. An estimate of the remaining background is obtained from an

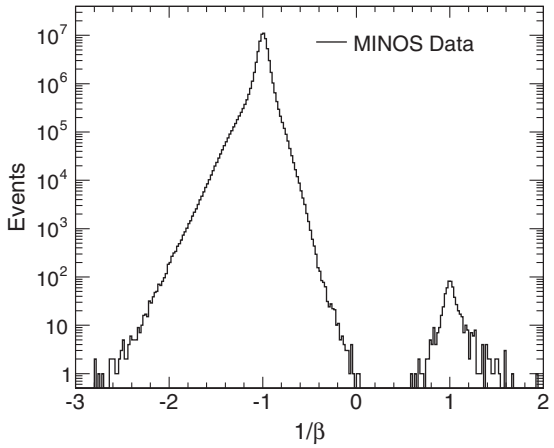

FIG. 4. Distribution of $1/\beta$ normalized velocity variable, demonstrating the purity of the track direction identification. The $1/\beta$ variable is the gradient of a linear fit to the measured times as a function of distance along each track. The distribution is plotted for all tracks that pass the topology and timing selections. The peak at -1.0 corresponds to downward-going muons; the peak at $+1.0$ to upward-going muons. A good separation is achieved between the upward-going neutrino-induced signal, and downward-going cosmic-ray muon background.

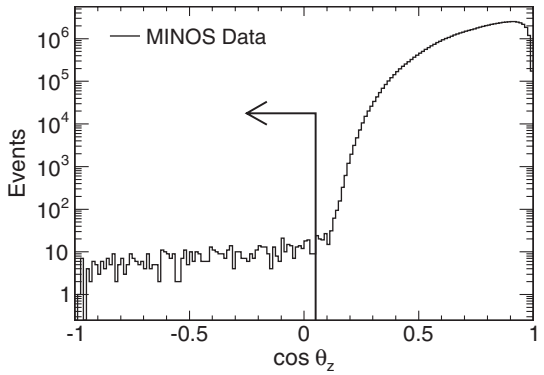

FIG. 5. Distribution of reconstructed zenith angle for muons with good timing and topology. In the range $\cos\theta_z > 0.10$, the observed rate of muons is dominated by the cosmic-ray background and falls steeply as the mean rock overburden increases rapidly. For $\cos\theta_z < 0.10$, the distribution flattens, as the cosmic-ray muon flux falls below that of neutrino-induced muons. To minimize the background from cosmic-ray muons, events are required to satisfy $\cos\theta_z < 0.05$.

exponential fit to observed data in the region $|\cos\theta_z| < 0.20$. This method returns a background prediction of 0.5 selected events. The cosmic-ray muon background component is neglected in the subsequent analysis.

Overall, 665 upward-going and horizontal muons are selected from the data. This compares with total predictions of 882 ± 146 events in the absence of oscillations, and 623 ± 113 events for input oscillation parameters of $\Delta m^2 = 2.32 \times 10^{-3}$ eV^2 and $\sin^2 2\theta = 1.0$, where the uncertainties are dominated by the normalizations of the contained-vertex and neutrino-induced rock-muon Monte Carlo simulations. The selected sample divides into 466 neutrino-induced rock-muons and 199 contained-vertex muons. The latter sample contains 95 events already selected as contained-vertex muons by the containment requirements described above, along with an additional 104 upward-going and horizontal events.

C. Selection of contained-vertex showers

The contained-vertex shower sample is primarily composed of the $\nu_e + \bar{\nu}_e$ CC and NC atmospheric neutrino component. For this sample, the main background arises from cosmic-ray muons incident at steep angles, which radiate large showers and span a small number of planes. The veto shield is first applied to reduce cosmic-ray muon background. The following selection criteria are then applied to the remaining showers [38]:

(1) *Fiducial and trace cuts.*—The fiducial requirements described above for contained-vertex tracks are also applied in the selection of contained-vertex showers. For reconstructed showers, the vertex resolution is poorer and cosmic-ray background level larger. Therefore, a tighter fiducial requirement of 0.4 m is applied at each edge of the detector for this sample. The shower direction also has a poorer resolution, and therefore a tighter trace cut of 0.8 m is applied. Figure 6 shows the predicted and observed Δ_Z distributions for contained-vertex showers.

(2) *Topology cuts.*—Further selection requirements are applied to identify the characteristic topologies of neutrino-induced showers. The longitudinal profile of these showers typically rises to a maximum and then falls smoothly, whereas showers generated by cosmic-ray muons typically deposit a lot of energy in a single plane, or contain large fluctuations between planes. The cosmic-ray background is also found to be higher for shorter showers. Therefore, events are separated into short (≤ 8 planes) and long (> 8 planes) samples, and tighter selection criteria are applied to the short sample. To characterize the shower topology, the mean and rms number of strips per plane ($\langle W_{UV}\rangle$ and $\langle W_{UV}^2\rangle^{\frac{1}{2}}$), and pulse height per plane ($\langle Q_{\rm shw}\rangle$ and $\langle Q_{\rm shw}^2\rangle^{\frac{1}{2}}$), are calculated. These shower topology variables are required to satisfy

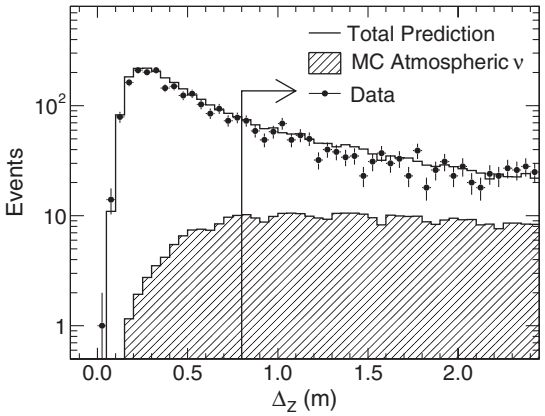

FIG. 6. Distributions of the trace variable, Δ_Z, for contained-vertex showers. This variable estimates the distance in z traveled by a cosmic-ray muon inside the detector before entering the scintillator. The hatched histogram shows the simulated prediction for the atmospheric neutrino signal. The solid line gives the predicted total rate, dominated by the cosmic-ray muon background. The points show the observed data. The background is peaked towards low values of Δ_Z, since cosmic-ray muons typically travel a small distance in z before entering the scintillator. The arrow indicates the selection applied on Δ_Z to reduce the background.

$$\langle W_{UV}\rangle < 5(4)\ \text{strips},$$
$$\langle W_{UV}^2\rangle^{\frac{1}{2}} < 4(3)\ \text{strips},$$
$$\langle Q_{\rm shw}\rangle < 150(100)\ \text{PEs},$$
$$\langle Q_{\rm shw}^2\rangle^{\frac{1}{2}} < 150(100)\ \text{PEs},$$

for long (short) showers, respectively. Figure 7 shows the predicted and observed distributions of the mean and rms shower pulse height variables. An analysis of the principal moments of the shower is also used to distinguish the showerlike event topology of atmospheric neutrinos from the tracklike topology of cosmic-ray muons. The moment of inertia tensor is constructed from the relative positions of the shower strips, weighted by their pulse height. The tensor is diagonalized and selection criteria are placed on the largest eigenvalue, $I_{UV}^{\rm max}$, with long (short) showers required to satisfy $I_{UV}^{\rm max} < 0.15(0.05)$ m^2, respectively.

(3) *Removal of selected tracks.*—After applying the above selection criteria, it is found that 2% of the resulting events have been previously selected as contained-vertex tracks. Monte Carlo studies indicate that approximately half of the duplicate events are ν_μ or $\bar{\nu}_\mu$ CC interactions. As a final step, these events are removed from the contained-vertex shower sample.

The shower containment requirements select 701 events from the data, compared with a total prediction of 727 ± 101 events in the absence of oscillations, and a prediction of 684 ± 95 events for oscillations with $\Delta m^2 = 2.32 \times 10^{-3}$ eV^2 and $\sin^2 2\theta = 1.0$. The uncertainties are

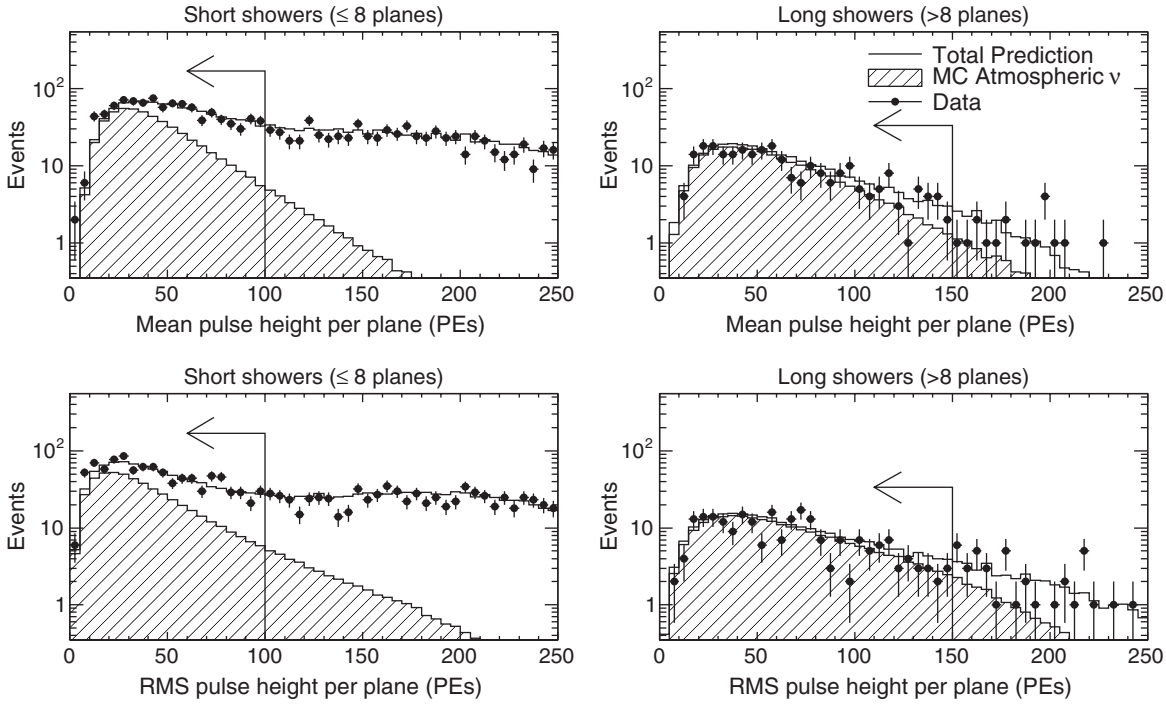

FIG. 7. Distributions of mean and rms shower pulse height per scintillator plane observed for contained-vertex showers that pass the fiducial and trace cuts. The hatched histogram shows the simulated prediction for the atmospheric neutrino signal. The solid line gives the total prediction, dominated by the cosmic-ray muon background. The points show the observed data. The arrows indicate the selection applied to reduce the background.

dominated by the 15% uncertainty in the overall normalization, but also includes additional uncertainties of 20% and 5% in the NC and $\nu_e + \bar{\nu}_e$ CC components, respectively. The cosmic-ray muon prediction of 87 ± 9 events represents a background level of 12%. Figure 8 shows the predicted and observed energy distributions of the selected events. Since the selected sample contains a small $\nu_\mu + \bar{\nu}_\mu$ CC component, the distribution has only a weak dependence on the oscillation parameters.

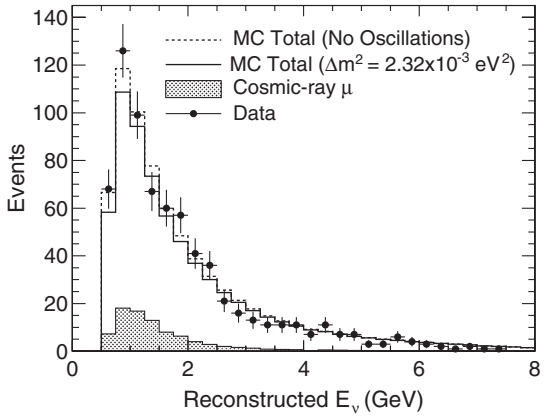

FIG. 8. Distributions of reconstructed neutrino energy, plotted for selected contained-vertex showers. The dotted line shows the prediction for no oscillations; the solid line shows the prediction for $\Delta m^2 = 2.32 \times 10^{-3}$ eV^2 and $\sin^2 2\theta = 1.0$; the shaded histogram shows the predicted cosmic-ray muon background; the points with errors show the observed data. The $\nu_\mu + \bar{\nu}_\mu$ CC component is small and hence the total prediction does not depend strongly on the oscillation parameters.

D. Summary of results from atmospheric neutrino event selection

In total, 2072 candidate atmospheric neutrino events are selected from the data. For analysis, the events are grouped into: 905 contained-vertex muons, with vertex positions inside the fiducial volume (including both fully contained and partially contained muons); 466 neutrino-induced rock-muons, with vertex positions outside the fiducial volume; and the 701 contained-vertex showers. Table I gives the predicted event rates for each of these samples.

E. Selection of high resolution event sample

A sample of high resolution contained-vertex muons, with well-measured muon propagation direction, is selected from the data. These high resolution events are required to satisfy minimum track length requirements of 10 planes and 1 m. They are also required to pass a timing requirement of $r_L - r_H < -0.66$ ns. These selection criteria are found to correctly distinguish the track direction in 99% of simulated atmospheric neutrinos.

A total of 631 high resolution contained-vertex muons are selected, with the remaining 274 contained-vertex muons classified as low resolution. In the high resolution

TABLE I. Summary of atmospheric neutrino selection, separated into the different categories of selected and simulated event. The Monte Carlo predictions are given separately for contained-vertex atmospheric neutrinos and neutrino-induced rock-muons, with the contained-vertex predictions also separated by neutrino interaction type. The cosmic muon background prediction is calculated directly from the data by weighting vetoed events according to the measured shield efficiency. In the top table, the predictions are calculated in the absence of neutrino oscillations; the bottom table uses representative oscillation parameters of $\Delta m^2 = 2.32 \times 10^{-3}$ eV^2 and $\sin^2 2\theta = 1.0$. The predictions and their uncertainties have been rounded to the nearest event. Note that many of the uncertainties are correlated and cancel in the ratios and fits described in this paper.

	Data	Prediction (no oscillations)						
		Cosmic-ray μ	$\nu_\mu + \bar{\nu}_\mu$ CC	$\nu_e + \bar{\nu}_e$ CC	$\nu_\tau + \bar{\nu}_\tau$ CC	NC	Rock-μ	Total
Contained-vertex muons	905	34 ± 3	998 ± 150	35 ± 6	...	25 ± 6	9 ± 2	1100 ± 159
Neutrino-induced rock-muons	466	...	26 ± 4	0 ± 0	...	0 ± 0	544 ± 136	570 ± 136
Contained-vertex showers	701	87 ± 9	157 ± 24	358 ± 57	...	124 ± 31	1 ± 0	727 ± 101
Total	2072			2397 ± 296				
	Data	Prediction ($\Delta m^2 = 2.32 \times 10^{-3}$ eV^2, $\sin^2 2\theta = 1.0$)						
		Cosmic-ray μ	$\nu_\mu + \bar{\nu}_\mu$ CC	$\nu_e + \bar{\nu}_e$ CC	$\nu_\tau + \bar{\nu}_\tau$ CC	NC	Rock-μ	Total
Contained-vertex muons	905	34 ± 3	689 ± 103	35 ± 6	3 ± 1	25 ± 6	6 ± 1	792 ± 113
Neutrino-induced rock-muons	466	...	14 ± 2	0 ± 0	0 ± 0	0 ± 0	433 ± 108	447 ± 108
Contained-vertex showers	701	87 ± 9	110 ± 16	358 ± 57	5 ± 2	124 ± 31	0 ± 0	684 ± 95
Total	2072			1923 ± 235				

sample, 261 events are classified as upward-going and 370 events are classified as downward-going. The measured up-down ratio is $R^{\text{data}}_{u/d} = 0.71 \pm 0.06(\text{stat})$, where the statistical error corresponds to the 68% confidence interval calculated using Poisson statistics [46]. The predicted ratio, calculated from the simulation, in the absence of oscillations, is $R^{\text{MC}}_{u/d} = 1.14 \pm 0.03(\text{syst})$. The 3% systematic uncertainty combines the uncertainties in the event selection, and the atmospheric neutrino flux simulation. The double ratio between the observed and predicted up-down ratio is

$$R^{\text{data}}_{u/d}/R^{\text{MC}}_{u/d} = 0.62 \pm 0.05(\text{stat}) \pm 0.02(\text{syst}).$$

This ratio is in excess of 6 standard deviations from unity, indicating the presence of neutrino oscillations.

VI. SEPARATION OF NEUTRINOS AND ANTINEUTRINOS

The high resolution contained-vertex muon sample and neutrino-induced rock-muon sample are separated into candidate neutrinos and antineutrinos based on the reconstructed muon charge sign. The Kalman filter returns a best fit value of q/p, and its uncertainty, $\sigma_{q/p}$, where q is the muon charge sign and p is the muon momentum. The selected events are classified as neutrinos if $q < 0$, and as antineutrinos if $q > 0$.

Two criteria are used to select events with significant track curvature and therefore well-measured charge sign. First, a requirement is placed on the relative size of the track fit uncertainty, $|q/p|/\sigma_{q/p}$, which indicates the significance of the track curvature [6]. Events are required to satisfy $|q/p|/\sigma_{q/p} > 2.5$. The reconstructed track is then used to calculate a variable measuring the straightness of the track, with the aim of excluding tracks which do not have significant curvature. A straight line is drawn between the reconstructed start and end point of the track, and a chi-squared variable, $\chi^2_{\text{line}}/\text{dof}$, is calculated from the deviations of the track strips from this line [7]. Events are required to satisfy $\chi^2_{\text{line}}/\text{dof} > 4.0$. Figure 9 shows the observed and predicted distributions of these two selection variables for contained-vertex muons and neutrino-induced rock-muons.

The charge selection criteria are found to correctly identify the muon charge in 97% of simulated contained-vertex interactions, and 99% of simulated neutrino-induced rock-muons. The selection efficiencies are 87% and 59%, respectively, calculated as a fraction of the number of selected events with well-measured direction. The lower efficiency for neutrino-induced rock-muons reflects their higher average momentum, resulting in more events with ambiguous track curvature.

Table II gives the predicted and observed numbers of neutrinos and antineutrinos for each category of event. For contained-vertex muons, the charge-separation procedure returns 379 neutrinos and 173 antineutrinos, giving a measured charge ratio of $R^{\text{data}}_{\bar{\nu}/\nu} = 0.46^{+0.05}_{-0.04}(\text{stat})$. The predicted value of the charge ratio is calculated from the simulation to be $R^{\text{MC}}_{\bar{\nu}/\nu} = 0.49 \pm 0.05(\text{syst})$. The prediction is almost entirely independent of any input oscillations, provided that equal parameters are used for neutrinos and antineutrinos. The overall systematic uncertainty of 10% is obtained by combining uncertainties of 8.5% in the ratio of the neutrino and antineutrino interaction cross sections, 4%

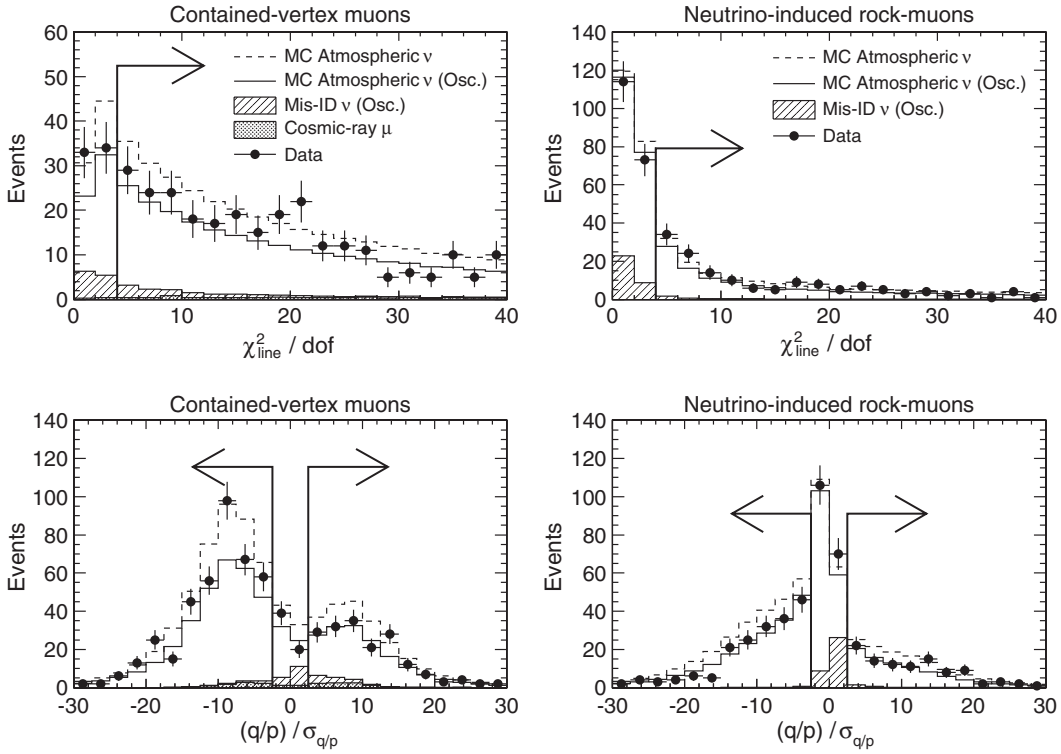

FIG. 9. Distributions of track fit uncertainty, $(q/p)/\sigma_{q/p}$, and track straightness variable, $\chi^2_{\text{line}}/\text{dof}$, used to select events with well-measured muon charge sign. The distributions are plotted for contained-vertex muons (left panels), and neutrino-induced rock-muons (right panels). In each plot, the dashed line indicates the total prediction in the absence of oscillations; the solid line shows the prediction for oscillations with $\Delta m^2 = 2.32 \times 10^{-3}$ eV^2 and $\sin^2 2\theta = 1.0$; the shaded histogram shows the cosmic-ray muon background; and the points show the observed data. In addition, the hatched histograms show the component with misidentified charge sign. The arrows indicate the selections used to identify events with well-measured charge sign.

in the flux ratio of neutrinos and antineutrinos, and 3% in the purity of the charge separation. The double ratio between the observed and predicted charge ratios is calculated to be $R^{\text{data}}_{\bar{\nu}/\nu}/R^{\text{MC}}_{\bar{\nu}/\nu} = 0.93 \pm 0.09(\text{stat}) \pm 0.09(\text{syst})$.

For neutrino-induced rock-muons, 152 neutrinos and 95 antineutrinos are selected, giving a measured charge ratio of $R^{\text{data}}_{\bar{\nu}/\nu} = 0.63^{+0.09}_{-0.08}(\text{stat})$. The predicted value of the charge ratio is calculated from the simulation to be

TABLE II. Results from the separation of contained-vertex and neutrino-induced rock-muons by reconstructed charge sign, into selected samples of neutrinos and antineutrinos. The predictions from each simulated sample are given separately for true neutrinos and antineutrinos; the column labeled "Other" is the sum of the cosmic-ray muon, $\nu_e + \bar{\nu}_e$, $\nu_\tau + \bar{\nu}_\tau$, and NC backgrounds. All the predictions and their uncertainties have been rounded to the nearest event. Note that many of the uncertainties are correlated and cancel in the ratios and fits described in this paper.

	Data	Prediction (no oscillations)					
		ν_μ CC	$\bar{\nu}_\mu$ CC	Rock-μ^-	Rock-μ^+	Other	Total
Contained-vertex muons (μ^-)	379	425 ± 64	4 ± 1	4 ± 1	0 ± 0	13 ± 1	445 ± 65
Contained-vertex muons (μ^+)	173	12 ± 2	190 ± 28	0 ± 0	1 ± 0	15 ± 2	219 ± 31
Neutrino-induced rock-muons (μ^-)	152	16 ± 2	0 ± 0	215 ± 54	1 ± 0	0 ± 0	233 ± 54
Neutrino-induced rock-muons (μ^+)	95	0 ± 0	8 ± 1	3 ± 1	102 ± 25	0 ± 0	112 ± 26
	Data	Prediction ($\Delta m^2 = 2.32 \times 10^{-3}$ eV^2, $\sin^2 2\theta = 1.0$)					
		ν_μ CC	$\bar{\nu}_\mu$ CC	Rock-μ^-	Rock-μ^+	Other	Total
Contained-vertex muons (μ^-)	379	294 ± 44	3 ± 0	2 ± 1	0 ± 0	15 ± 2	314 ± 46
Contained-vertex muons (μ^+)	173	9 ± 1	132 ± 20	0 ± 0	1 ± 0	16 ± 2	158 ± 22
Neutrino-induced rock-muons (μ^-)	152	9 ± 1	0 ± 0	151 ± 38	1 ± 0	0 ± 0	161 ± 38
Neutrino-induced rock-muons (μ^+)	95	0 ± 0	4 ± 1	2 ± 0	68 ± 17	0 ± 0	74 ± 18

$R^{\mathrm{MC}}_{\bar{\nu}/\nu} = 0.48 \pm 0.06(\mathrm{syst})$. The overall systematic uncertainty of 12.5% is obtained by combining uncertainties of 10% in the flux ratio, 4% in the cross-section ratio, and 6% in the charge-separation purity. The double ratio between the observed and predicted charge ratio is $R^{\mathrm{data}}_{\bar{\nu}/\nu}/R^{\mathrm{MC}}_{\bar{\nu}/\nu} = 1.29^{+0.19}_{-0.17}(\mathrm{stat}) \pm 0.16(\mathrm{syst})$.

The charge-separated samples of contained-vertex muons and neutrino-induced rock-muons are combined to give an overall double ratio of

$$R^{\mathrm{data}}_{\bar{\nu}/\nu}/R^{\mathrm{MC}}_{\bar{\nu}/\nu} = 1.03 \pm 0.08(\mathrm{stat}) \pm 0.08(\mathrm{syst}).$$

This result is consistent with unity.

VII. OSCILLATION ANALYSIS

Two oscillation fits are applied to the selected data. The first is a two-parameter fit, which outputs equal oscillation parameters for neutrinos and antineutrinos; the second is a four-parameter fit, which outputs separate oscillation parameters for neutrinos and antineutrinos. Each fit is applied to the reconstructed L/E distributions of selected neutrinos and antineutrinos. The neutrino propagation length, L, is determined from the reconstructed zenith angle of the muon track. For contained-vertex muons, the parent neutrino energy, E, is found by summing the reconstructed muon energy and visible shower energy. For neutrino-induced rock-muons, only the muon energy is used, due to the increased uncertainties in the shower simulation and calibration at the edge of the detector, or because the interaction occurs outside the detector and hence the vertex is not visible. Figure 10 shows the predicted and observed reconstructed zenith angle distributions for contained-vertex muons and neutrino-induced rock-muons. Figures 11 and 12 show the predicted and observed L/E distributions for these two samples, before and after the separation of events into neutrinos and antineutrinos. For each of these figures, the observed data are compared

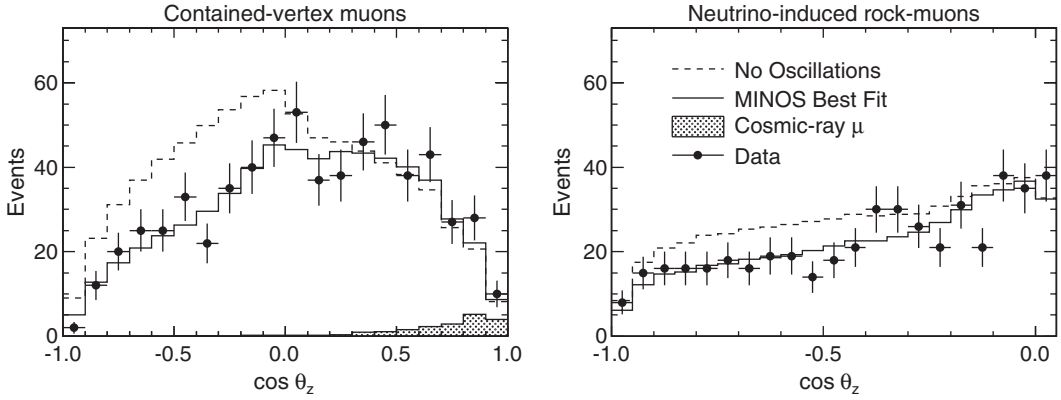

FIG. 10. Distributions of reconstructed zenith angle, for contained-vertex muons (left), and neutrino-induced rock-muons (right). In each plot, the dashed line gives the nominal prediction for the case of no oscillations; the shaded histogram shows the cosmic-ray muon background; and the points with errors show the observed data. The solid line shows the best fit to the data, which combines the best fit oscillation and systematic parameters.

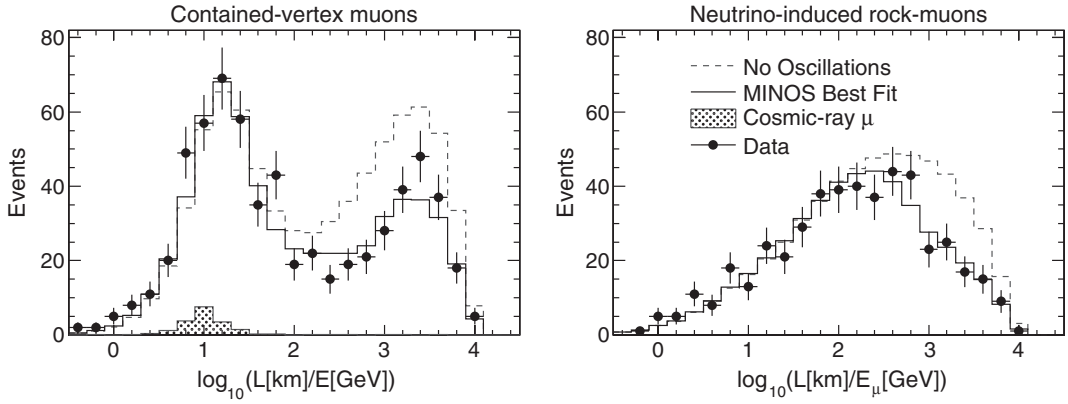

FIG. 11. Distributions of reconstructed $\log_{10}(L/E)$, for contained-vertex muons (left), and neutrino-induced rock-muons (right). In each plot, the dashed line gives the nominal prediction for the case of no oscillations; the shaded histogram shows the cosmic-ray muon background; and the points with errors show the observed data. The solid line shows the best fit to the data, which combines the best fit oscillation and systematic parameters.

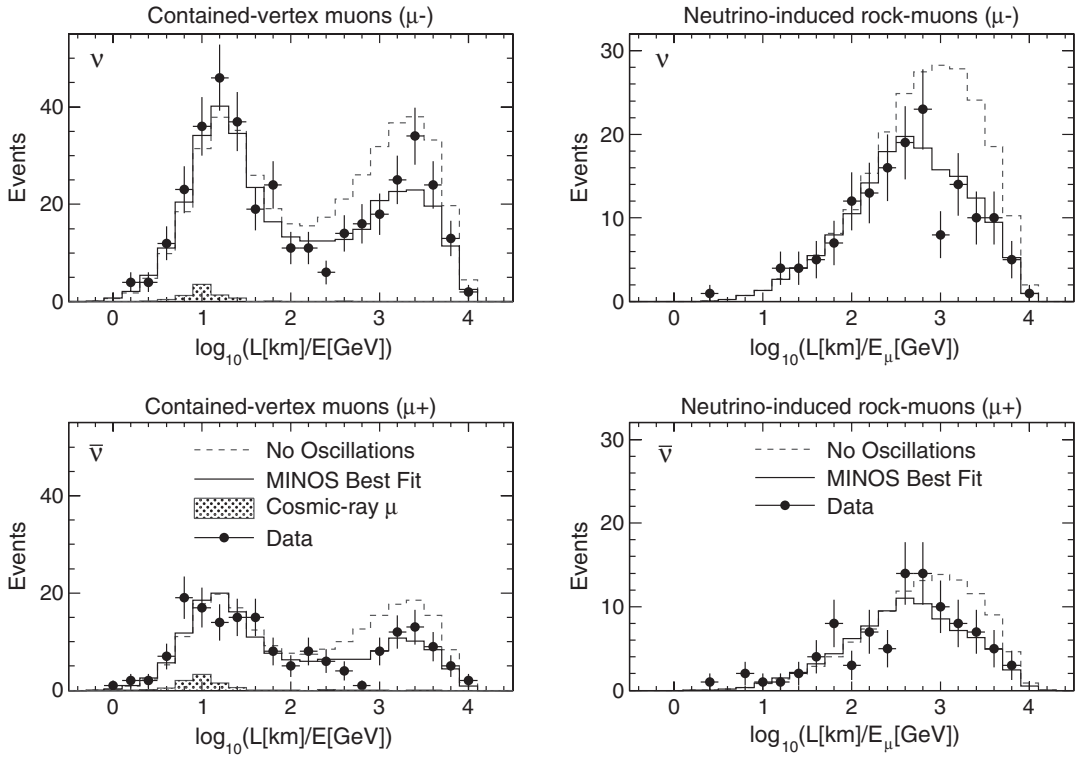

FIG. 12. Distributions of reconstructed $\log_{10}(L/E)$, plotted for selected neutrinos and antineutrinos in the contained-vertex muon sample (left panels) and neutrino-induced rock-muon sample (right panels). In each case, the dashed line gives the nominal prediction in the absence of oscillations; the shaded histogram shows the cosmic-ray muon background; and the points with errors show the observed data. The solid line indicates the best fit to the data, which combines the best fit oscillation and systematic parameters.

with the best fit neutrino and antineutrino oscillation parameters, which are given in Sec. VIII.

A. Separation of events by L/E resolution

The intrinsic L/E resolution of contained-vertex events, and therefore the degree to which they contribute to the overall sensitivity to the oscillation parameters, varies significantly across the high resolution sample. The resolution in the propagation distance depends on the reconstructed energy and zenith angle, and is worse at low energies where the average angle between the neutrino and muon is large, and also around the horizon where the propagation distance varies rapidly as a function of zenith angle. The resolution in the neutrino energy is worse for events where the muon momentum is determined from curvature rather than range, and also for events with high y values, since the shower energy resolution is generally poorer than the muon momentum resolution.

The sensitivity to oscillations can be improved by incorporating information on L/E resolution into the oscillation fit. For this analysis, a Bayesian technique is used to estimate the L/E resolution of selected contained-vertex muons on an event-by-event basis. For each event, a probability distribution function (PDF) in $\log_{10}(L/E)$ is calculated by combining the measured muon momentum, muon direction, and shower energy of the event with information from the Monte Carlo simulation describing the atmospheric neutrino spectrum, interaction kinematics, and detector resolution. The simulation is used to construct PDFs relating the measured muon momentum and shower energy of selected ν_μ and $\bar{\nu}_\mu$ events to their corresponding true distributions. The simulation also provides PDFs in the kinematic variables W^2 and y for ν_μ and $\bar{\nu}_\mu$ CC interactions, binned as a function of neutrino energy, which enable the distributions of muon momentum and shower energy to be mapped onto a distribution of neutrino energy, and the muon direction to be mapped onto a distribution of neutrino zenith angle. The overall PDF in $\log_{10}(L/E)$ is then obtained by taking a convolution of these neutrino distributions and the rms of this PDF, $\sigma_{\log(L/E)}$, gives the L/E resolution. A full description of the technique is given in [47].

Figure 13 shows the predicted and observed $\sigma_{\log(L/E)}$ distributions for high resolution contained-vertex muon neutrinos. The shape of the predicted distribution is almost independent of the input oscillation parameters. The observed spread of $\sigma_{\log(L/E)}$ values is substantial, and corresponds to 25% of the spread in $\log_{10}(L/E)$. Therefore, a significant gain in sensitivity is expected by separating events into bins of L/E resolution.

For the oscillation analysis, the selected contained-vertex muon neutrinos are divided into the following four bins of L/E resolution:

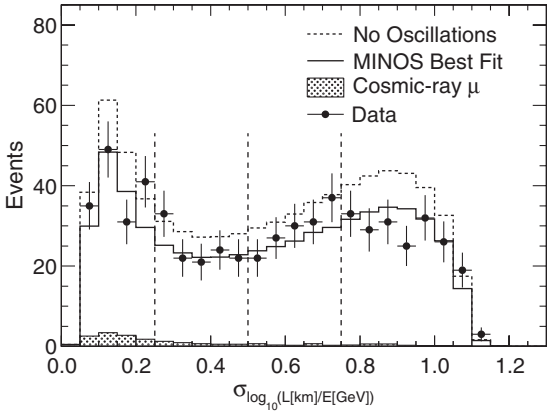

FIG. 13. Distributions showing the calculated L/E resolution for the high resolution sample of contained-vertex muon, which have well-measured propagation direction. The dashed histogram indicates the nominal prediction in the absence of oscillations; the solid histogram indicates the prediction for the best fit oscillation parameters presented in this paper; the shaded histogram shows the cosmic-ray muon background; and the points with error bars represent the observed data. The vertical dashed lines correspond to the partitions used to divide the selected events into four bins of L/E resolution.

$$0.00 \leq \sigma_{\log(L/E)} < 0.25,$$
$$0.25 \leq \sigma_{\log(L/E)} < 0.50,$$
$$0.50 \leq \sigma_{\log(L/E)} < 0.75,$$
$$0.75 \leq \sigma_{\log(L/E)} < 1.50.$$

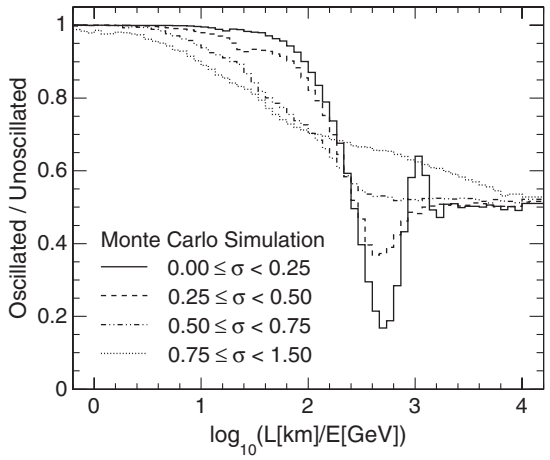

FIG. 14. Ratios of the predicted $\log_{10}(L/E)$ distributions with oscillations to those without oscillations in the four bins of L/E resolution. The predictions with oscillations are generated using input parameters of $\Delta m^2 = 2.32 \times 10^{-3}$ eV^2 and $\sin^2 2\theta = 1.0$. The oscillations are most sharply defined in the bin of highest resolution. Here, a clear oscillation dip can be seen at $\log_{10}(L/E) \approx 2.7$, corresponding to the peak oscillation probability. The ratio then rises to a maximum at $\log_{10}(L/E) \approx 3$, and a second dip is visible before the ratio averages to $1 - \frac{1}{2}\sin^2 2\theta = 0.5$, as the frequency of oscillations becomes rapid.

Figure 14 shows the ratio of the predicted L/E distributions with oscillations to those without oscillations in each bin of resolution. The oscillations are most sharply resolved in the bin with the best L/E resolution. Here, the ratio initially falls with L/E, reaching a minimum at the peak oscillation probability. The ratio subsequently rises to a maximum, and a second oscillation dip is visible before the ratio averages to $1 - \frac{1}{2}\sin^2 2\theta$ as the frequency of oscillations becomes rapid.

Selected neutrino-induced rock-muons are separated into low momentum ($P_\mu \leq 10$ GeV) and high momentum ($P_\mu > 10$ GeV) samples. This separation roughly distinguishes those muons whose parent neutrinos have a relatively large oscillation probability from those with a lower probability.

Figure 15 shows the predicted and observed L/E distributions, separated into bins of L/E resolution for contained-vertex muons, and into bins of muon momentum for neutrino-induced rock-muons. The predicted distributions are calculated for the case of no oscillations, and for the best fit neutrino and antineutrino oscillation parameters.

B. Oscillation fit

An oscillation fit is applied to the data assuming two-flavor $\nu_\mu \rightarrow \nu_\tau$ vacuum oscillations. In this approximation, the oscillation probability is given by

$$P(\nu_\mu \rightarrow \nu_\tau) = \sin^2 2\theta \sin^2\left(\frac{\Delta m^2 L}{4E}\right),$$

where Δm^2 and $\sin^2 2\theta$ are the two-flavor oscillation parameters, L is the neutrino propagation distance, and E is the neutrino energy.

For upward-going atmospheric neutrinos with energies in the 2–20 GeV region, an asymmetry between muon neutrinos and antineutrinos is predicted, arising from the resonant enhancement of three-flavor oscillations by matter effects [48]. The sign of the asymmetry depends on the sign of the neutrino squared-mass difference, and is therefore sensitive to the mass ordering of neutrinos [49]. These effects have only a small influence on the predicted L/E distributions of neutrinos and antineutrinos and so are not considered in this analysis.

The high and low resolution contained-vertex muons, neutrino-induced rock-muons, and contained-vertex showers are each included as separate samples in the oscillation fit. For the low resolution contained-vertex muons and contained-vertex shower samples, the events are fitted in single bins of normalization. The high resolution contained-vertex muon sample is divided into two bins of direction, $r = (u, d)$, corresponding to upward-going (u) and downward-going (d) muons; three bins of charge sign, $s = (\nu, \bar{\nu}, X)$, corresponding to neutrinos (ν), antineutrinos ($\bar{\nu}$), and events with ambiguous charge sign (X); and four bins of L/E resolution. The neutrino-induced rock-muon sample is divided into three bins of charge sign, and two

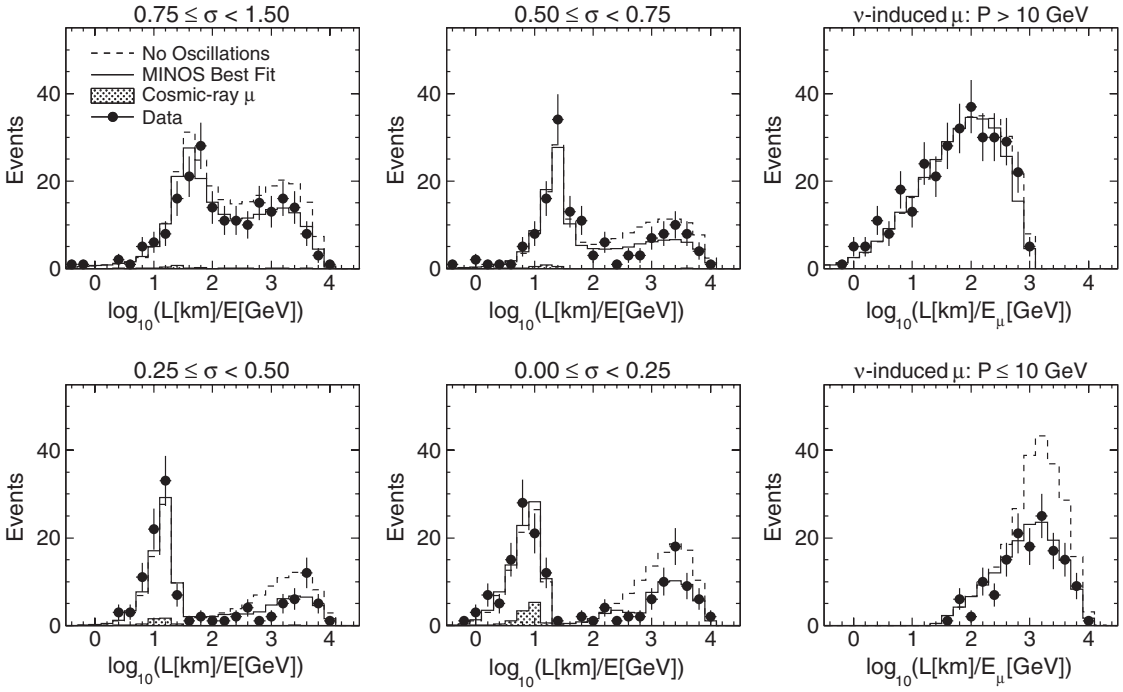

FIG. 15. Distributions of $\log_{10}(L/E)$ observed in each bin of L/E resolution for contained-vertex muons, and in each bin of muon momentum for neutrino-induced rock-muons. For each of the panels, the dashed line gives the nominal prediction in the absence of oscillations; the shaded histogram shows the cosmic-ray muon background; and the points represent the data. The solid line indicates the best fit to the data, combining the best fit oscillation and systematic parameters.

bins of muon momentum. Overall, there are 24 high resolution contained-vertex muon and 6 neutrino-induced rock-muon distributions. Each distribution is binned in $\log_{10}(L/E)$, using 25 bins in the range $[-0.5, +4.5]$. This gives a total of 750 high resolution bins, in addition to the 2 low resolution bins.

A maximum likelihood fit to the data is performed using the following negative log-likelihood function:

$$-\ln\mathcal{L} = \sum_l \mu - n\ln\mu + \sum_h \sum_{r,s} \mu - n\ln\mu - \sum_h \sum_{r,s} \sum_{i,k} n_{ik}\ln(f_{ik}) + \sum_j \frac{\alpha_j^2}{2\sigma_{\alpha_j}^2}.$$

This log-likelihood function is divided into the following terms:

(1) *Normalization.*—The sums $\sum \mu - n\ln\mu$ represent the Poisson probability for observing a total of n events with a prediction of μ events. The first sum, denoted l, is taken over the contained-vertex shower and low resolution contained-vertex muon samples, which are fitted in single bins; the second sum, denoted h, is taken over the neutrino-induced rock-muon and high resolution contained-vertex muon samples, which are separated by muon direction $r = (u, d)$ and charge sign $s = (\nu, \bar{\nu}, X)$.

(2) *Shape term.*—The shape of the $\log_{10}(L/E)$ distribution is incorporated into the oscillation fit for the neutrino-induced rock-muon and high resolution contained-vertex muon samples. The terms $\sum_{i,k} n_{ik}\ln(f_{ik})$ represent the likelihood functions for each of the $\log_{10}(L/E)$ distributions included in the fit. The i sum is taken over each resolution bin for the contained-vertex muons, and each momentum bin for neutrino-induced rock-muons; the k sum is taken over each of the 25 bins in the $\log_{10}(L/E)$ distribution. Within the sum, n_{ik} is the observed number of events and f_{ik} is the relative predicted probability in the ith and kth bins.

(3) *Systematic uncertainties.*—Systematic effects are incorporated as nuisance parameters, where the shift α_j is the deviation of the jth systematic parameter from its nominal value. A penalty term, $\alpha_j^2/2\sigma_{\alpha_j}^2$, is added to the likelihood, where the error σ_{α_j} represents the estimated uncertainty in the jth systematic parameter.

A total of 12 systematic uncertainties are incorporated into the fit as nuisance parameters, as listed in Table III. For contained-vertex neutrino interactions, a 15% uncertainty is applied to the normalization of the event sample. The following additional uncertainties are applied to this sample: a 3% uncertainty on the up-down ratio; a 5% uncertainty on the $(\nu_\mu + \bar{\nu}_\mu)/(\nu_e + \bar{\nu}_e)$ ratio; a 10% uncertainty on the $\bar{\nu}_\mu/\nu_\mu$ ratio; and a 20% uncertainty on the ratio of NC to CC interactions. For neutrino-induced rock-muons,

TABLE III. Summary of systematic uncertainties included in the oscillation fit, along with the best fit oscillation and systematic parameters returned by each fit. For the two-parameter fit, equal oscillation parameters are used for neutrinos and antineutrinos; for the four-parameter fit, separate oscillation parameters are used. The best fit systematic parameters are given in units of standard deviations.

Parameter	Uncertainty	Best fit (2 oscillation parameters)	Best fit (4 oscillation parameters)
$\lvert\Delta m^2\rvert/\mathrm{eV}^2$		1.9×10^{-3}	2.2×10^{-3}
$\lvert\Delta \bar{m}^2\rvert/\mathrm{eV}^2$		1.9×10^{-3}	1.6×10^{-3}
$\sin^2 2\theta$		0.99	0.99
$\sin^2 2\bar{\theta}$		0.99	1.00
Normalization (contained-vertex ν)	$\sigma = 15\%$	$+0.6\sigma$	$+0.7\sigma$
Normalization (ν-induced rock-μ)	$\sigma = 25\%$	$+0.1\sigma$	$+0.1\sigma$
up/*down* ratio (contained-vertex ν)	$\sigma = 3\%$	-0.1σ	-0.1σ
ν_e/ν_μ ratio (contained-vertex ν)	$\sigma = 5\%$	-0.5σ	-0.5σ
$\bar{\nu}_\mu/\nu_\mu$ ratio (contained-vertex ν)	$\sigma = 10\%$	-0.5σ	-0.6σ
$\bar{\nu}_\mu/\nu_\mu$ ratio (ν-induced rock-μ)	$\sigma = 12.5\%$	$+1.1\sigma$	$+0.9\sigma$
NC/*CC* ratio (contained-vertex ν)	$\sigma = 20\%$	$+0.6\sigma$	$+0.6\sigma$
ν spectrum parameter	$\sigma = 6\%$	-0.4σ	-0.4σ
$\bar{\nu}$ spectrum parameter	$\sigma = 6\%$	$+0.3\sigma$	$+0.3\sigma$
μ momentum (range)	$\sigma = 3\%$	-0.3σ	-0.3σ
μ momentum (curvature)	$\sigma = 5\%$	$+0.3\sigma$	$+0.3\sigma$
Shower energy	$\sigma = 15\%$	$+0.4\sigma$	$+0.4\sigma$

a 25% uncertainty is applied on the normalization of the event sample. An additional 12.5% uncertainty is applied to the $\bar{\nu}_\mu/\nu_\mu$ ratio in this sample.

To account for the uncertainty in the shape of the atmospheric neutrino energy spectrum, the number of contained-vertex events is allowed to scale as a function of neutrino energy. The form of the scaling function is chosen to cover the variations in the spectrum generated by changing the flux model and by reweighting the cross-section model according to its given uncertainties. Above 3 GeV, where the prediction from the simulation approximately follows a power function, events are scaled by $f(E_\nu) = 1 + \alpha \ln(E_\nu/3)$. Below 3 GeV, this is connected smoothly to a linear function, $f(E_\nu) = 1 + \alpha(E_\nu - 3)$. The scaling function is applied separately to neutrinos and antineutrinos. In each case, the spectrum parameter, α, is normally distributed with a standard deviation of 6%. Finally, to account for the systematic uncertainties on the track and shower energy scale, a 3% uncertainty is included on the muon momentum from range, 5% on the momentum from curvature, and 15% on the shower energy scale. Of all the systematic uncertainties incorporated into the fit, only the two normalization parameters are found to have a significant impact on the resulting confidence limits.

C. Results of oscillation fit

The log-likelihood function is minimized with respect to the oscillation and nuisance parameters. Table III summarizes the best fit parameters. The best fit point occurs at $(|\Delta m^2|, \sin^2 2\theta) = (1.9 \times 10^{-3}\ \mathrm{eV}^2, 0.99)$. The 68%, 90%, and 99% confidence limits (C.L.) on the oscillation parameters are obtained in the limit of Gaussian errors from the locus of points with log-likelihood values of $-\Delta \ln \mathcal{L} = (1.15, 2.30, 4.61)$ relative to the best fit point. Figure 16 shows the resulting 90% contours from this analysis. For comparison, this figure also shows the 90% contours from the MINOS beam neutrino analysis [12], and also from the Super-Kamiokande atmospheric neutrino zenith angle analysis [21].

The log-likelihood surface is used to calculate single-parameter confidence intervals for each of the oscillation

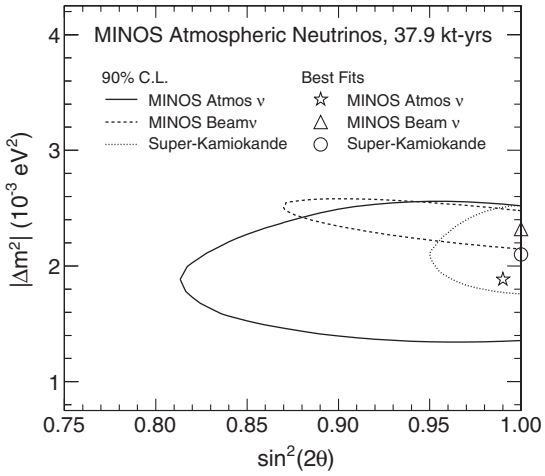

FIG. 16. Confidence limits on the parameters $|\Delta m^2|$ and $\sin^2 2\theta$, assuming equal oscillations for neutrinos and antineutrinos. The solid line gives the 90% contour obtained from this analysis, with the best fit parameters indicated by the star. For comparison, the dashed line shows the 90% contour given by the MINOS oscillation analysis of neutrinos from the NuMI beam [12], with the best fit point indicated by the triangle. The dotted line shows the 90% contour from the Super-Kamiokande atmospheric neutrino zenith angle analysis (from [21]), with the best fit point indicated by the circle.

parameters, by minimizing with respect to the other oscillation parameter. The 90% single-parameter confidence intervals at the best fit point, calculated using this method, are $|\Delta m^2| = (1.9 \pm 0.4) \times 10^{-3}$ eV^2 and $\sin^2 2\theta > 0.86$. The null oscillation hypothesis is disfavored at the level of 9.2 standard deviations.

VIII. FITS TO NEUTRINO AND ANTINEUTRINO OSCILLATIONS

Since the data are separated into pure samples of neutrinos and antineutrinos, they can be used to study oscillations separately in neutrinos and antineutrinos. The analysis described above is extended to incorporate separate oscillation parameters for neutrinos $(\Delta m^2, \sin^2 2\theta)$ and for antineutrinos $(\Delta \bar{m}^2, \sin^2 2\bar{\theta})$. The log-likelihood function is then minimized with respect to these oscillation parameters and the 12 nuisance parameters. The best fit occurs at $(|\Delta m^2|, \sin^2 2\theta) = (2.2 \times 10^{-3}$ eV$^2, 0.99)$ and $(|\Delta \bar{m}^2|, \sin^2 2\bar{\theta}) = (1.6 \times 10^{-3}$ eV$^2, 1.00)$, as given in Table III. The neutrino and antineutrino oscillation parameters are found to be approximately uncorrelated around the best fit point. A set of two-parameter profiles can be calculated from the four-parameter likelihood surface by minimizing with respect to pairs of oscillation parameters. Figure 17 shows the resulting 90% contours obtained for the $(|\Delta m^2|, \sin^2 2\theta)$ and $(|\Delta \bar{m}^2|, \sin^2 2\bar{\theta})$ planes. These results are compared with the 90% contours from the MINOS analyses of NuMI beam data acquired in neutrino [12] and antineutrino [15] mode, and also the 90% contours from the SK analysis of atmospheric neutrinos and antineutrinos [21].

The four-parameter likelihood surface is used to calculate single-parameter confidence intervals on each of the four oscillation parameters. The resulting 90% C.L. are: $|\Delta m^2| = 2.2^{+2.4}_{-0.6} \times 10^{-3}$ eV^2 and $\sin^2 2\theta > 0.83$ for neutrinos; and $|\Delta \bar{m}^2| = 1.6^{+0.5}_{-0.5} \times 10^{-3}$ eV^2 and $\sin^2 2\bar{\theta} > 0.76$ for antineutrinos. The null oscillation hypothesis is disfavored at the level of 7.8 standard deviations for neutrinos and 5.4 standard deviations for antineutrinos.

As a measure of the quality of the fit, a set of 10 000 simulated experiments were generated at the best fit oscillation parameters. For each simulated experiment, input systematic parameters were chosen from Gaussian PDFs with widths set to the systematic uncertainties. The best fit parameters were then found for each experiment by minimizing the log-likelihood function. For each experiment, the minimum value of $-\Delta \ln \mathcal{L}$ was recorded; in 22% of experiments, the value exceeded that obtained from the fit to the data.

Figure 18 compares the observed 90% C.L. from each fit with the predictions from the Monte Carlo simulation, calculated by inputting the best fit oscillation parameters into the simulation. For the two-parameter oscillation fit, where neutrinos and antineutrinos take the same oscillation parameters, there is good agreement between the observed and predicted contours. For the four-parameter oscillation fit, where neutrinos and antineutrinos take separate oscillation parameters, there is a good match between contours for the limits on the $\sin^2 2\theta$ and $\sin^2 2\bar{\theta}$ parameters and the lower limits on the $|\Delta m^2|$ and $|\Delta \bar{m}^2|$ parameters. However, the upper limits on these parameters are found to be higher than predicted for neutrinos and lower than predicted for antineutrinos.

As a check on the observed confidence limits, the full likelihood surface was calculated for a set of 250 simulated experiments, generated at the best fit oscillation parameters from the two-parameter fit. The resulting 90% confidence intervals were then calculated for each experiment. In 25% of these experiments, the confidence intervals obtained for

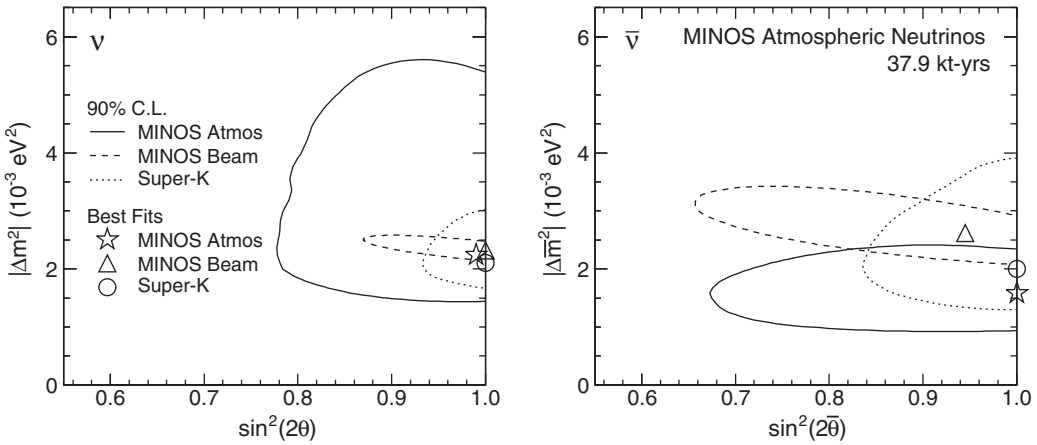

FIG. 17. Confidence limits on neutrino (left) and antineutrino (right) oscillation parameters. The solid lines show the 90% contours obtained from this analysis. The two-parameter contours for neutrinos and antineutrinos are calculated by profiling the four-parameter likelihood surface. The best fit parameters are indicated by the stars. For comparison, the dashed lines in each plot show the 90% contours from the MINOS analysis of beam data in neutrino mode [12] and antineutrino mode [15], with the best fit points indicated by the triangles. The dotted lines show the 90% contours from the Super-Kamiokande analysis of atmospheric neutrinos and antineutrinos (from [21]), with the best fit points indicated by the circles.

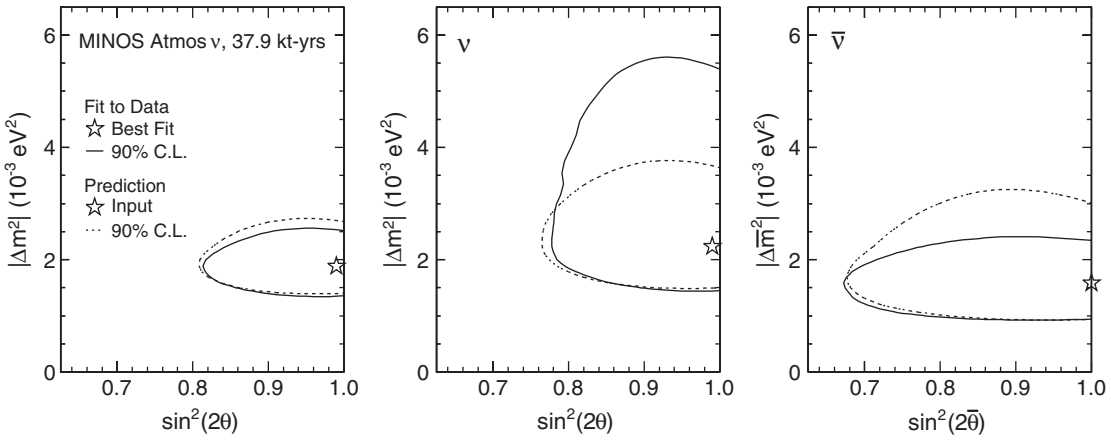

FIG. 18. Comparisons of the observed and predicted 90% contours. The left plot shows the contours for the two-parameter oscillation fit, where neutrinos and antineutrinos take the same oscillation parameters. The right two plots, labeled ν and $\bar{\nu}$, show the contours obtained for neutrinos and antineutrinos, respectively, resulting from the four-parameter oscillation fit, where neutrinos and antineutrinos take different oscillation parameters. In each case, the predicted contours are generated by inputting the best fit parameters from the observed data into the simulation, and running the full oscillation fit, including the 12 systematic parameters.

the Δm^2 parameter are broader for neutrinos than antineutrinos, as is the case for the observed data; in 10% of the experiments, the relative size of these intervals is larger than for the observed data. These results indicate that the confidence intervals calculated from the observed data are reasonable.

Finally, a log-likelihood profile is calculated in the $(|\Delta m^2|, |\Delta \bar{m}^2|)$ plane, by minimizing the log-likelihood function with respect to the $\sin^2 2\theta$ and $\sin^2 2\bar{\theta}$ parameters. Figure 19 shows the resulting 68%, 90%, and 99% confidence intervals. This log-likelihood profile is used to place limits on the difference between the neutrino and antineutrino mass splittings $|\Delta m^2|$ and $|\Delta \bar{m}^2|$. The single-parameter 90% confidence intervals, assuming Gaussian errors, are $|\Delta m^2| - |\Delta \bar{m}^2| = 0.6^{+2.4}_{-0.8} \times 10^{-3}$ eV^2. This result is consistent with equal mass splittings for neutrinos and antineutrinos.

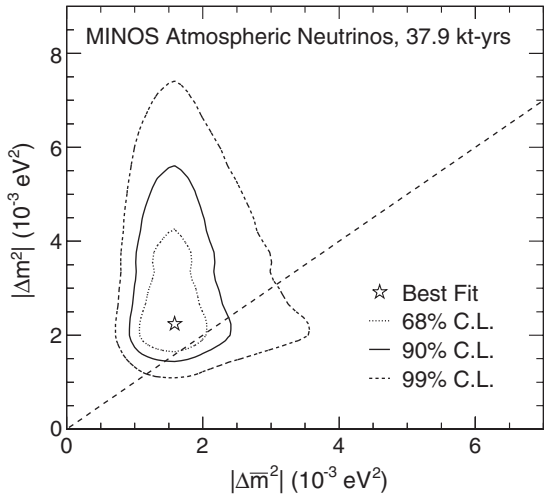

FIG. 19. Confidence limits obtained for the oscillation parameters $|\Delta m^2|$ and $|\Delta \bar{m}^2|$, representing the mass splittings for neutrinos and antineutrinos, respectively. At each point in parameter space, the negative log-likelihood function has been minimized with respect to the mixing parameters $\sin^2 2\theta$ and $\sin^2 2\bar{\theta}$. The 68%, 90%, and 99% contours are indicated by the dotted, solid, and dashed curves, respectively, and the best fit parameters are indicated by the star. The diagonal dashed line indicates the line of $|\Delta m^2| = |\Delta \bar{m}^2|$.

IX. SUMMARY

The 5.4 kton MINOS Far Detector has been collecting atmospheric neutrino data since August 2003. An analysis of the 2553 live-days of data collected up to March 2011 yields a total of 2072 candidate atmospheric neutrino events. The events are separated into 905 contained-vertex muons and 466 neutrino-induced rock-muons, produced by ν_μ and $\bar{\nu}_\mu$ CC interactions, and 701 contained-vertex showers, composed primarily of ν_e and $\bar{\nu}_e$ CC interactions and NC interactions. The curvature of muons in the magnetic field is used to divide the selected contained-vertex muons and neutrino-induced rock-muons into separate samples of ν_μ and $\bar{\nu}_\mu$ events. The double $\bar{\nu}_\mu/\nu_\mu$ ratio is calculated to be $R^{\text{data}}_{\bar{\nu}/\nu}/R^{\text{MC}}_{\bar{\nu}/\nu} = 1.03 \pm 0.08(\text{stat}) \pm 0.08(\text{syst})$.

A maximum likelihood fit to the observed L/E distributions is used to determine the atmospheric neutrino oscillation parameters. The sensitivity to oscillations is improved by separating the contained-vertex muons into bins of L/E resolution, and the neutrino-induced rock-muons into bins of muon momentum. The fit returns 90% confidence limits of $|\Delta m^2| = (1.9 \pm 0.4) \times 10^{-3}$ eV^2 and $\sin^2 2\theta > 0.86$. The oscillation fit is extended to allow separate oscillation parameters for neutrinos and antineutrinos. This fit returns 90% confidence limits of $|\Delta m^2| - |\Delta \bar{m}^2| = 0.6^{+2.4}_{-0.8} \times 10^{-3}$ eV^2 on the difference between the squared-mass splittings for neutrinos and antineutrinos, consistent with equal mass splittings for neutrinos and antineutrinos.

ACKNOWLEDGMENTS

This work was supported by the U.S. DOE, the U.K. STFC, the U.S. NSF, the State and University of Minnesota, the University of Athens in Greece, and Brazil's FAPESP and CNPq. We are grateful to the Minnesota Department of Natural Resources, the crew of Soudan Underground Laboratory, and the staff of Fermilab, for their contributions to this effort.

[1] Y. Ashie *et al.* (Super-Kamiokande Collaboration), Phys. Rev. Lett. **93**, 101801 (2004).
[2] Y. Ashie *et al.* (Super-Kamiokande Collaboration), Phys. Rev. D **71**, 112005 (2005).
[3] K. Abe *et al.* (Super-Kamiokande Collaboration), Phys. Rev. Lett. **97**, 171801 (2006).
[4] M. Ambrosio *et al.* (MACRO Collaboration), Eur. Phys. J. C **36**, 323 (2004).
[5] W. W. M. Allison *et al.* (Soudan 2 Collaboration), Phys. Rev. D **72**, 052005 (2005).
[6] P. Adamson *et al.* (MINOS Collaboration), Phys. Rev. D **73**, 072002 (2006).
[7] P. Adamson *et al.* (MINOS Collaboration), Phys. Rev. D **75**, 092003 (2007).
[8] M. H. Ahn *et al.* (K2K Collaboration), Phys. Rev. D **74**, 072003 (2006).
[9] K. Abe *et al.* (T2K Collaboration), Phys. Rev. D **85**, 031103 (2012).
[10] D. G. Michael *et al.* (MINOS Collaboration), Phys. Rev. Lett. **97**, 191801 (2006).
[11] P. Adamson *et al.* (MINOS Collaboration), Phys. Rev. Lett. **101**, 131802 (2008).
[12] P. Adamson *et al.* (MINOS Collaboration), Phys. Rev. Lett. **106**, 181801 (2011).
[13] P. Adamson *et al.* (MINOS Collaboration), Phys. Rev. D **84**, 071103 (2011).
[14] P. Adamson *et al.* (MINOS Collaboration), Phys. Rev. Lett. **107**, 021801 (2011).
[15] P. Adamson *et al.* (MINOS Collaboration), Phys. Rev. Lett. **108**, 191801 (2012).
[16] K. Anderson *et al.*, Report No. FERMILAB-DESIGN-1998-01, 1998.
[17] J. Kopp, P. A. N. Machado, and S. J. Parke, Phys. Rev. D **82**, 113002 (2010).
[18] W. A. Mann, D. Cherdack, W. Musial, and T. Kafka, Phys. Rev. D **82**, 113010 (2010).
[19] M. C. Gonzalez-Garcia, M. Maltoni, and T. Schwetz, Phys. Rev. D **68**, 053007 (2003).
[20] G. Barenboim and J. D. Lykken, Phys. Rev. D **80**, 113008 (2009).
[21] K. Abe *et al.* (Super-Kamiokande Collaboration), Phys. Rev. Lett. **107**, 241801 (2011).
[22] B. Rebel, Ph.D. thesis, University of Indiana, 2004.
[23] D. G. Michael *et al.* (MINOS Collaboration), Nucl. Instrum. Methods Phys. Res., Sect. A **596**, 190 (2008).
[24] P. Adamson *et al.* (MINOS Collaboration), Phys. Rev. D **76**, 052003 (2007).
[25] H. Gallagher, Nucl. Phys. B, Proc. Suppl. **112**, 118 (2002).
[26] T. Gabriel and C. Zeitnitz, Nucl. Instrum. Methods Phys. Res., Sect. A **349**, 106 (1994).
[27] D. Casper, Nucl. Phys. B, Proc. Suppl. **112**, 161 (2002).
[28] M. Gluck, E. Reya, and A. Vogt, Z. Phys. C **67**, 433 (1995).
[29] S. Giani *et al.*, CERN Program Library Long Writeup, Report No. W5013 (unpublished).
[30] G. D. Barr, T. K. Gaisser, P. Lipari, S. Robbins, and T. Stanev, Phys. Rev. D **70**, 023006 (2004).
[31] V. Agrawal, T. K. Gaisser, P. Lipari, and T. Stanev, Phys. Rev. D **53**, 1314 (1996).
[32] University of New Hampshire, Neutron Monitor Datasets, National Science Foundation Grant No. ATM- 9912341.
[33] G. D. Barr, S. Robbins, T. K. Gaisser, and T. Stanev, Phys. Rev. D **74**, 094009 (2006).
[34] G. Battistoni, A. Ferrari, T. Monturuli, and P. Sala, Astropart. Phys. **19**, 269 (2003).
[35] M. Honda, T. Kajita, K. Kasahara, S. Midorikawa, and T. Sanuki, Phys. Rev. D **75**, 043006 (2007).
[36] P. Adamson *et al.* (MINOS Collaboration), Phys. Rev. D **81**, 072002 (2010).
[37] H. Gallagher (private communication).
[38] B. Speakman, Ph.D. thesis, University of Minnesota, 2007.
[39] A. Blake, Ph.D. thesis, University of Cambridge, 2005.
[40] J. Marshall, Ph.D. thesis, University of Cambridge, 2008.
[41] A. Culling, Ph.D. thesis, University of Cambridge, 2007.
[42] C. Howcroft, Ph.D. thesis, University of Cambridge, 2004.
[43] J. Chapman, Ph.D. thesis, University of Cambridge, 2007.
[44] M. Crouch, in *Proceedings of the 20th International Cosmic Ray Conference (ICRC), Moscow, USSR, 1987*, edited by V. Kozyarivsky *et al.* (Nauka, USSR, 1987), Vol. 6, p. 165.
[45] D. DeMuth *et al.* (Soudan 2 Collaboration), Astropart. Phys. **20**, 533 (2004).
[46] N. Gehrels, Astrophys. J. **303**, 336 (1986).
[47] A. S. T. Blake, J. D. Chapman, and M. A. Thomson, arXiv:1208.2899.
[48] L. Wolfenstein, Phys. Rev. D **17**, 2369 (1978).
[49] S. Palomares-Ruiz and S. Petcov, Nucl. Phys. **B712**, 392 (2005).